ISSN 2770-5900 (Online)
Volume 2 | Issue 1 | February 2022

Energy Materials

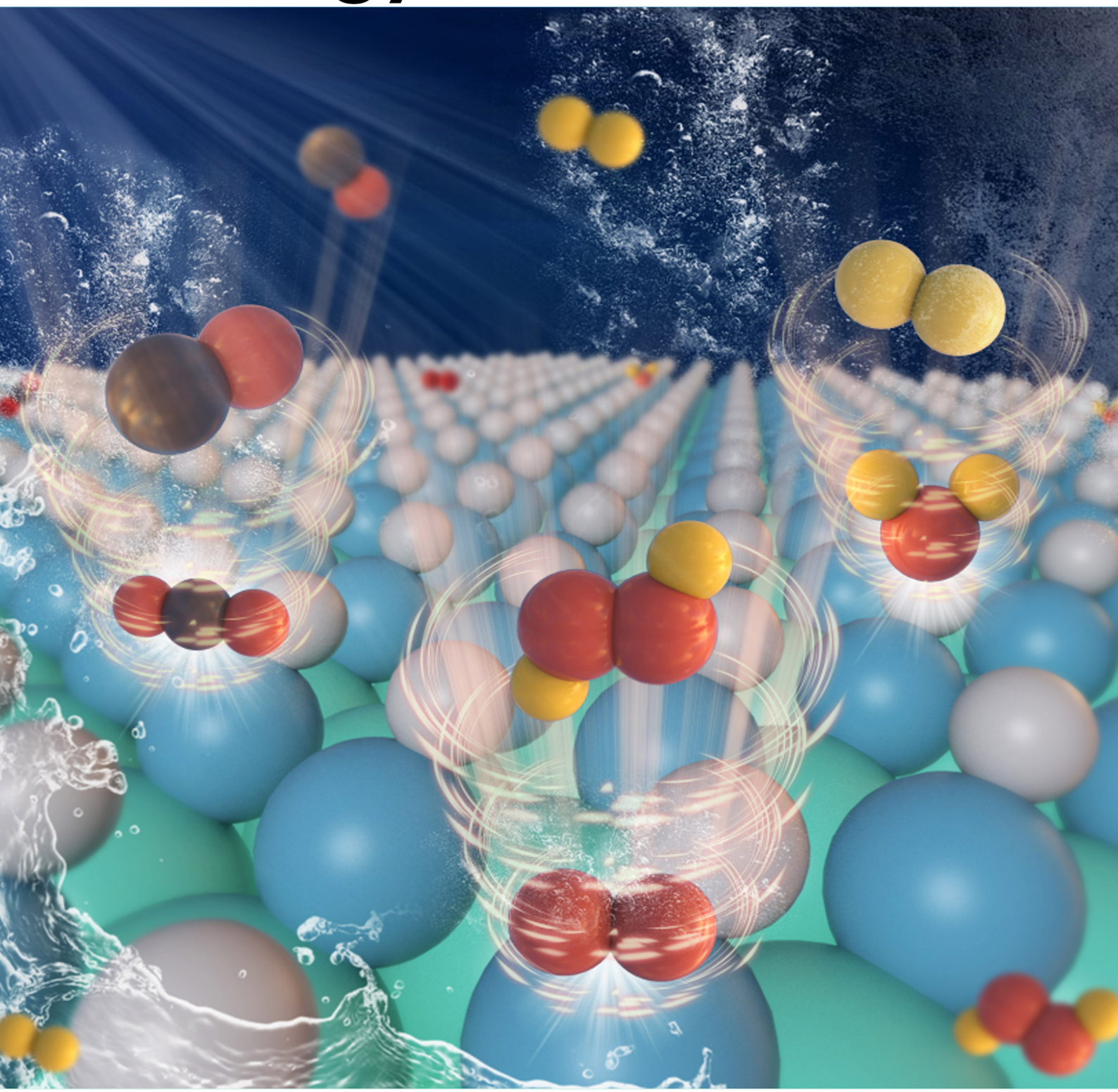

Open Access

www.energymaterj.com

Chen *et al. Energy Mater* 2022;2:200001
DOI: 10.20517/energymater.2021.24

Energy Materials

Review

Open Access

Recent advances in photocatalytic renewable energy production

Xiaolang Chen[#], Jingjing Zhao[#], Guisheng Li, Dieqing Zhang*, Hexing Li*

The Education Ministry Key Lab of Resource Chemistry, Shanghai Key Laboratory of Rare Earth Functional Materials, Shanghai Frontiers Science Center of Biomimetic Catalysis, College of Chemistry and Materials Science, Shanghai Normal University, Shanghai, 200234, China.
[#]Authors contributed equally.

***Correspondence to:** Prof. Dieqing Zhang, the Education Ministry Key Lab of Resource Chemistry, Shanghai Key Laboratory of Rare Earth Functional Materials, Shanghai Frontiers Science Center of Biomimetic Catalysis, College of Chemistry and Materials Science, Shanghai Normal University, No. 100, Guilin Road, Xuhui District, Shanghai, 200234, China.
E-mail: happy2002zdq@126.com; Prof. Hexing Li, the Education Ministry Key Lab of Resource Chemistry, Shanghai Key Laboratory of Rare Earth Functional Materials, Shanghai Frontiers Science Center of Biomimetic Catalysis, College of Chemistry and Materials Science, Shanghai Normal University, No. 100, Guilin Road, Xuhui District, Shanghai, 200234, China.
E-mail: hexing-li@shnu.edu.cn

How to cite this article: Chen X, Zhao J, Li G, Zhang D, Li H. Recent advances in photocatalytic renewable energy production. *Energy Mater* 2022;2:200001. https://dx.doi.org/10.20517/energymater.2021.24

Received: 26 Nov 2021 **First Decision:** 29 Dec 2021 **Revised:** 11 Jan 2022 **Accepted:** 19 Jan 2022 **Published:** 29 Jan 2022

Academic Editors: Yuping Wu, Yuhui Chen **Copy Editor:** Xi-Jun Chen **Production Editor:** Xi-Jun Chen

Abstract

The development of green and renewable energy is becoming increasingly more important in reducing environmental pollution and controlling CO_2 discharge. Photocatalysis can be utilized to directly convert solar energy into chemical energy to achieve both the conversion and storage of solar energy. On this basis, photocatalysis is considered to be a prospective technology to resolve the current issues of energy supply and environmental pollution. Recently, several significant achievements in semiconductor-based photocatalytic renewable energy production have been reported. This review presents the recent advances in photocatalytic renewable energy production over the last three years by summarizing the typical and significant semiconductor-based and semiconductor-like photocatalysts for H_2 production, CO_2 conversion and H_2O_2 production. These reactions demonstrate how the basic principles of photocatalysis can be exploited for renewable energy production. Finally, we conclude our review of photocatalytic renewable energy production and provide an outlook for future related research.

Keywords: Photocatalysis, solar energy conversion, renewable energy, semiconductors

INTRODUCTION

The overconsumption of fossil fuels has depleted traditional energy resources and contributed to environmental pollution in water, soil and air environments[1]. It is highly expected that renewable and green energy can be exploited to resolve the energy crisis and environmental pollution. Solar energy is an extremely attractive natural energy source. The amount of solar energy that hits the Earth's surface each year (1.3×10^5 TW) is much greater than that consumed by humans (1.6×10^1 TW in 2010)[2,3]. The conversion of solar energy to chemical energy via chemical reactions is a prospective method of producing renewable energy. Inspired by the natural photosynthesis of green plants and some other microorganisms, which convert solar energy to chemical energy in the form of carbohydrates or hydrogen, artificial photosynthesis (photocatalysis) is considered a prospective technology for the conversion of solar energy to chemical energy[4-6]. Since Fujishima and Honda discovered water photolysis on TiO_2 electrodes in 1972, photocatalysis has received tremendous attention and developed rapidly in recent decades due to its promising applications in renewable energy production[7,8].

The basic principles of semiconductor-based photocatalysis are presented in Figure 1[9]. In general, a complete photocatalytic process on a semiconductor involves three steps. The first step is light absorption, where photons are absorbed by the semiconductor photocatalyst. If the energy (hv) of the photons is larger than the bandgap energy of the semiconductor, the electrons (e^-) are excited and transmitted to the conduction band (CB) from the valence band (VB), leaving holes (h^+) in the VB. Pairs of negatively charged electrons and positively charged holes (e^--h^+ pairs) are generated in this step. The second step is charge separation and transfer. The photogenerated e^--h^+ pairs are separated and transferred to the surface of the semiconductor, while some photogenerated e^- and h^+ recombine in the bulk of the photocatalyst (volume recombination). The final step is surface reduction and oxidation reactions. The photogenerated charges on the surface of the semiconductor react with chemical species[9,10]. Meanwhile, some photogenerated e^- and h^+ recombine without taking part in any chemical reaction (surface recombination).

Realizing the efficient conversion of solar energy to chemical energy for the production of renewable energy relies on semiconductor photocatalysts[11]. One of the major issues associated with semiconductor photocatalysts is the insufficient rate of light utilization. The positions of the band edge (CB and VB) in a semiconductor should meet the required potentials of redox reactions. However, this means that light with a lower energy than the absorption onset [visible or even near-infrared (NIR) light] cannot be used. In addition, semiconductor photocatalysts suffer from the inefficient separation of photogenerated charge carriers, resulting in poor photoactivity and quantum efficiency[11]. There are two effective strategies for overcoming these issues. The first is the development of semiconductor photocatalysts with excellent light absorption ability to improve the light utilization rate. The second is the construction of a scheme or system (including cocatalysts) to effectively facilitate the separation of photogenerated e^--h^+ pairs. Current state-of-the-art semiconductor-based nanocomposite systems (e.g., materials with element doping/single atom modification, the construction of heterostructures and the development of cocatalysts) offer intense and wide absorption of light from across the solar spectrum, as well as highly efficient charge separation. These achievements have contributed greatly to the field of renewable energy production.

Herein, we introduce the advances in photocatalytic renewable energy production made in the last three years. We demonstrate how the basic principles of photocatalysis are used in certain reactions for renewable energy production, such as photocatalytic H_2 production, CO_2 conversion and H_2O_2 production, and

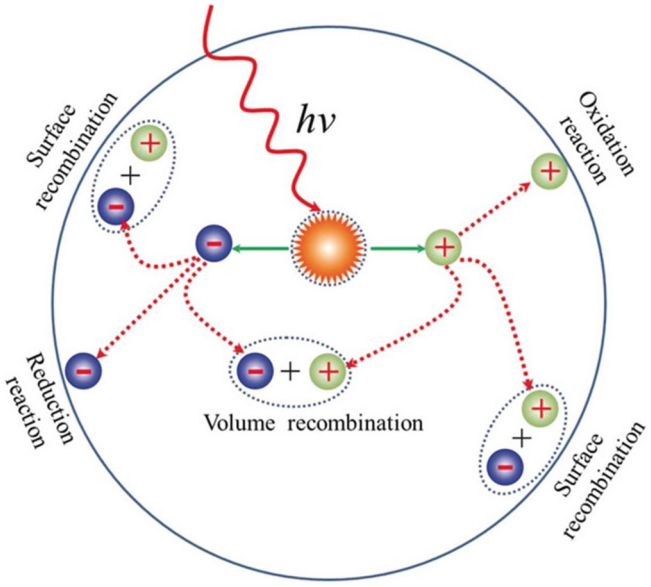

Figure 1. Basic principles of semiconductor-driven photocatalysis. Reproduced from Ref.[9] with permission from Wiley.

introduce some of the typical heterogeneous photocatalysts used in these reactions, such as inorganic semiconductors and organic semiconductor-like materials (e.g., metal- and covalent-organic frameworks). Finally, we conclude with the progression made in photocatalytic renewable energy production and provide an outlook for future related research.

PHOTOCATALYTIC RENEWABLE ENERGY PRODUCTION

Photocatalytic H_2 production

Basic principles of photocatalytic H_2 production

H_2 is a promising clean energy source that does not produce secondary pollution[12]. After light harvesting and the separation and transfer of the photogenerated e^--h^+ pairs in the aforementioned principle of photocatalysis, the photogenerated e^- in the CB reduce adsorbed H^+ to H_2 [Figure 2] and the photogenerated h^+ in the VB oxidize a sacrificial agent (S), such as alcohols (e.g., CH_3OH, CH_3CH_2OH and $CH_3CH_2CH_2OH$), triethanolamine (TEOA) or triethylamine (TEA) into an oxidative product (S^+) or water into oxygen (O_2)[13-15]. Nonetheless, the energy level of CB for the H_2 evolution reaction should be lower than 0 V *vs.* the normal hydrogen electrode (NHE) at pH 7. Additionally, the energy level of the VB for the H_2O oxidation reaction should be higher than 1.23 V *vs.* NHE, as the following redox reactions show:

Reduction reaction:

$2H^+ + 2e^- \rightarrow H_2$ $E = 0.00$ eV(1)

Oxidation reaction:

Sacrificial agent (S) + $h^+ \rightarrow S^+$ $E > 1.23$ eV(2)

or

$H_2O + 2h^+ \rightarrow ½O_2 + 2H^+$ $E = 1.23$ eV(3)

Overall water splitting:

$2H_2O \rightarrow O_2 + 2H_2$ $E = -1.23$ eV(4)

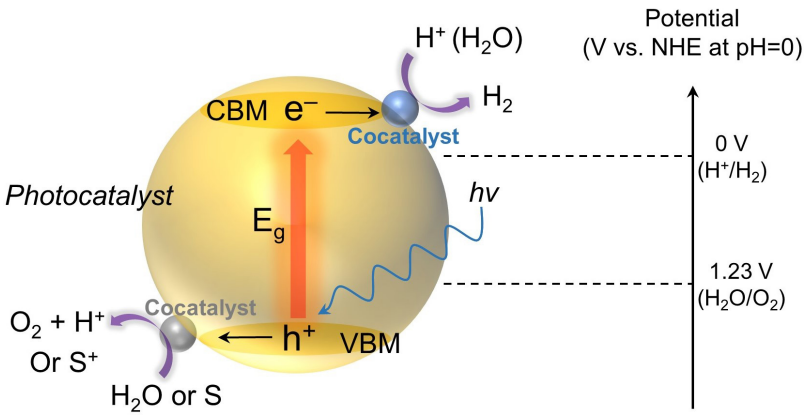

Figure 2. Schematic energy diagram of photocatalytic H_2 production from water-splitting on a semiconductor photocatalyst. CBM: Conduction band minimum; VBM: valence band maximum; E_g: bandgap energy.

Recent advances in photocatalytic H_2 production

H_2 production from water with sacrificial agents

I. Metal oxide-based photocatalysts

Metal oxides have the advantages of low cost, good structural stability and low toxicity. In addition, they are easy to prepare and can be modified via various strategies, which can impart them with improved performances. Moreover, the proper band positions confer metal oxides with good redox capability in the photocatalytic H_2 production reaction[16].

Titanium dioxide (TiO_2) is the most frequently investigated semiconductor material for photocatalytic H_2 production. Hejazi *et al.*[17] described an atomic-scale defect engineering method to form and control traps for Pt single atom (SA) sites upon thin sputtered TiO_2 layers for photocatalytic H_2 production. The density of defect centers can be precisely regulated, resulting in the controlled density of Pt SA sites on TiO_2. These decorated Pt SA sites improved the photoactivity of TiO_2 by 150 times compared to that on conventional Pt nanoparticle-modified TiO_2. Cho *et al.*[18] reported that a pre-reduced TiO_2 support, which can reverse the interaction with Pt nanoparticles and reinforce the metallic state of Pt, resulting in a three-fold increase in H_2 production rate compared to that on traditional Pt/TiO_2. Pt/TiO_2/H_2O triple junctions are the active catalytic sites for H_2 production in the presence of CH_3OH. Méndez-Medrano *et al.*[19] constructed a heterojunction between small CuO nanoclusters and TiO_2 (P25), which induces a photocatalytic activity of H_2 production by using CH_3OH as a sacrificial agent under visible-light irradiation because of the narrow bandgap (1.7 eV) of CuO. The photogenerated e^- was injected from CuO nanoclusters to the CB of TiO_2 (P25), resulting in high photoactivity. Osuagwu *et al.*[20] presented anatase TiO_2 nanosheet (NS) layers grown on a Ta_2O_5 substrate and this TiO_2 NSs/Ta_2O_5 displayed a 170-fold increase in photocatalytic H_2 production rate compared to that on TiO_2 NSs on a fluorine-doped tin oxide (FTO) substrate with CH_3OH as a sacrificial agent. Such drastically enhanced photoactivity can be ascribed to the blocking effect of Ta_2O_5 for the photogenerated e^- in TiO_2 NSs.

Sun *et al.*[21] synthesized a dodecahedral N-doped C-coated CuO-In_2O_3 p-n heterojunction photocatalyst, which showed a photocatalytic H_2 production rate of 600 μmol·g^{-1}·h^{-1} and good long-term stability of 50 h in a TEOA aqueous solution. Such a photocatalytic H_2 production rate can be attributed to the efficient separation of photogenerated e^--h^+ pairs and the mediated adsorption behavior ($|\Delta G_{H^*}|\rightarrow 0$) by coupling the N-doped C layer with the CuO-In_2O_3 p-n heterojunction. The improved stability may originate from the mitigation of electron deficiency in CuO by the formation of the p-n heterojunction and protection with the

N-doped C layer. In 2021, Han *et al.*[22] proposed a rhombohedral corundum/cubic In_2O_3 (rh/c-In_2O_3) phase-junction photocatalyst, which could effectively promote the separation and transfer of photogenerated charges between rh-In_2O_3 and c-In_2O_3 with a Z-scheme mechanism. This In_2O_3 phase-junction photocatalyst showed a H_2 production rate of 2244 μmol·g^{-1}·h^{-1} in a TEOA aqueous solution. A relevant apparent quantum efficiency (AQE) of 35% was achieved at 400 nm, which is ~12 times that on bare c-In_2O_3.

II. Sulfide-based photocatalysts

Sulfides, such as molybdenum disulfide (MoS_2), zinc sulfide (ZnS), cadmium sulfide (CdS) and tungsten sulfide (WS_2), have been developed for photocatalytic H_2 production.

In 2018, Guo *et al.*[23] reported a MoS_2@TiO_2 catalyst for photocatalytic H_2 production. The catalyst realized a H_2 production rate of 580 mmol·$g_{MoS}$$^{-1}$·$h^{-1}$ under simulated solar light irradiation, while methanol was used as a sacrificial hole scavenger. The heterostructure between plasmonic MoS_2 and TiO_2 regulated the charge transfer pathways, which were responsible for light harvesting and photocatalytic H_2 production. Wang *et al.*[24] embedded edge-enriched ultrathin MoS_2 flake cocatalysts into a yolk-shell TiO_2 bulk to boost photogenerated e^- transfer from the bulk to the TiO_2 surface. The as-prepared MoS_2/TiO_2 hybrid showed a H_2 production rate of 2443 μmol·g^{-1}·h^{-1}, which is ~10- and ~4.7-fold greater than that of pure TiO_2 (247 μmol·g^{-1}·h^{-1}) and bulk MoS_2-modified TiO_2 (513 μmol·g^{-1}·h^{-1}), respectively. This improved activity was ascribed to the exposed catalytic edges of the ultra-thin MoS_2 cocatalysts with strong Ti-S bonds, offering a fast charge-transfer pathway between TiO_2 and MoS_2. Furthermore, WS_2-MoS_2 in-plane few-layer heterostructures that function as efficient photocatalysts have been developed recently[25]. The built-in potential at the epitaxially-grown WS_2-MoS_2 interface facilitated fast separation of the photogenerated e^--h^+ pairs, resulting in a H_2 production rate of 9.83 mmol·g^{-1}·h^{-1}.

Xiao *et al.*[26] fabricated a copper nanowire (CuNW)/ZnS hybrid with a core-shell structure by a microwave-assisted hydrothermal route [Figure 3A]. The obtained ZnS with a narrowed bandgap could form a strong coupled interface with the CuNWs. As a result, this catalyst exhibited improved activity and stability for photocatalytic H_2 production under the illumination of visible light [Figure 3B and C]. The corresponding H_2 production rate reached 10,722 μmol·g^{-1}·h^{-1} with an AQE of 69% under LED illumination with a wavelength (λ) of 420 nm. Cu^+ ions from the CuNWs doped the ZnS shell, lowering the Schottky barrier and enabling photogenerated e^- to be injected from Cu^+/ZnS to the CuNWs, resulting in efficient charge separation. The core-shell NW structure benefited reactant absorption, charge separation and active site protection. Specifically, the CuNW cores acted as active sites to accept e^- for the efficient reduction of H^+ to H_2 [Figure 3D and E].

Wang *et al.*[27] prepared a zinc oxide/CdS hierarchical composite. The CdS moiety plays a key role in light harvesting. A photocatalytic H_2 production rate of 4134 μmol·g^{-1}·h^{-1} was obtained with Na_2S and Na_2SO_3 as electron donors. The Z-scheme charge migration scheme bestowed the photocatalyst with a strong ability for H_2 production and improved the photoactivity. Dai *et al.*[28] constructed a system composed of a unique pyroelectric substrate, poly(vinylidene fluoride-*co*-hexafluoropropylene), carbon nanotubes and a CdS photocatalyst for infrared (IR)-light-driven H_2 production in the presence of TEA. The photocatalytic H_2 production efficiency was improved by more than five times with an AQE of 16.9%. Zhang *et al.*[29] first converted Cd-based Prussian blue analog cubes into a CdS cage, which were then further transformed into a CdS frame-in-cage. Owing to the novel frame-in-cage structure, a visible-light-driven H_2 production rate of 13.6 mmol·g^{-1}·h^{-1} was achieved while Na_2S and Na_2SO_3 were used as sacrificial hole scavengers, which was much higher compared to that of the CdS cubes and cages.

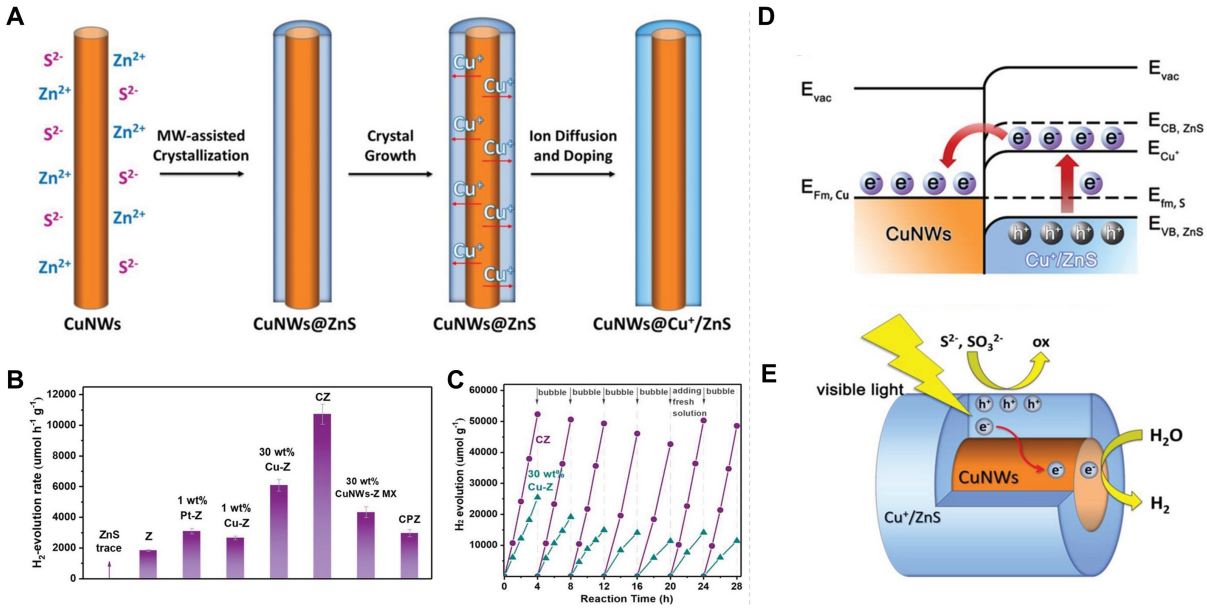

Figure 3. (A) Schematic illustration of CuNW/ZnS core-shell hybrids formed by a microwave-assisted hydrothermal route. (B) Photocatalytic H_2 production rate of different samples under LED light irradiation (λ = 420 nm). (C) Cycling activity of CZ and 30 wt.% Cu-Z. (D) Schottky contact, band structure and schematic illustration of the e^--h^+ separation process under visible-light irradiation. (E) Schematic diagram of the core-shell structure and the proposed photocatalytic mechanism. Reproduced from Ref.[26] with permission from Wiley.

III. Carbon nitride-based photocatalysts

Carbon nitride (C_3N_4) comprises only earth-abundant C and N elements and has high thermal and chemical stability because of the robust covalent bonds between the C and N atoms in the layered structure [Figure 4][30,31]. Its bandgap energy is ~2.7 eV, meaning that it can absorb visible light. In addition, the CB and VB edge positions of C_3N_4 are suitable for water reduction and oxidation, respectively[32-34]. Therefore, C_3N_4 is a promising photocatalyst.

In 2019, Mo *et al.*[35] proposed a Z-scheme system containing two-dimensional (2D) MnO_2/monolayer graphitic carbon nitride with defective Mn^{3+} active sites for H_2 production, while TEOA was used as a sacrificial agent. After Mn^{3+}/Mn^{4+} redox couples were introduced, these defective Mn^{3+} active sites could promote H_2O adsorption and boost the charge separation and transfer at the interface, resulting in a H_2 production rate of 28.0 mmol·g^{-1}·h^{-1} and an AQE of 23.33% at λ = 420 nm. Wang *et al.*[36] prepared Se-doped carbon nitride (Se-C_3N_4) by fluorination, followed by thermal defluorination in Se vapor to realize 2D C_3N_4 with a strong visible-light absorption band. The formation of cyano groups accompanied by Se doping expanded the absorption edge of the C_3N_4 from 416 to 584 nm. In addition, a downward electron spin polarization in the C_3N_4 structure facilitated charge separation and surface catalysis reactions. The visible-light-driven H_2 production rate reached 5411.2 μmol·g^{-1}·h^{-1} using Se-C_3N_4 with 3 wt.% Pt as a cocatalyst, which was 176.5 times that of the pure C_3N_4 in the presence of TEOA.

In 2021, Xu *et al.*[37] prepared a NIR-active C/K-doped red polymeric carbon nitride (RPCN). The homogeneous and high incorporation of C and K narrowed the bandgap of C_3N_4 (1.7 eV), thus extending the light absorption edge to the NIR region [Figure 5A]. RPCN displayed a NIR-driven H_2 production rate of 140 μmol·g^{-1}·h^{-1} from water [Figure 5B and C]. The AQE was 0.84% at 700 ± 10 nm and 13% at 500 ± 10 nm [Figure 5D].

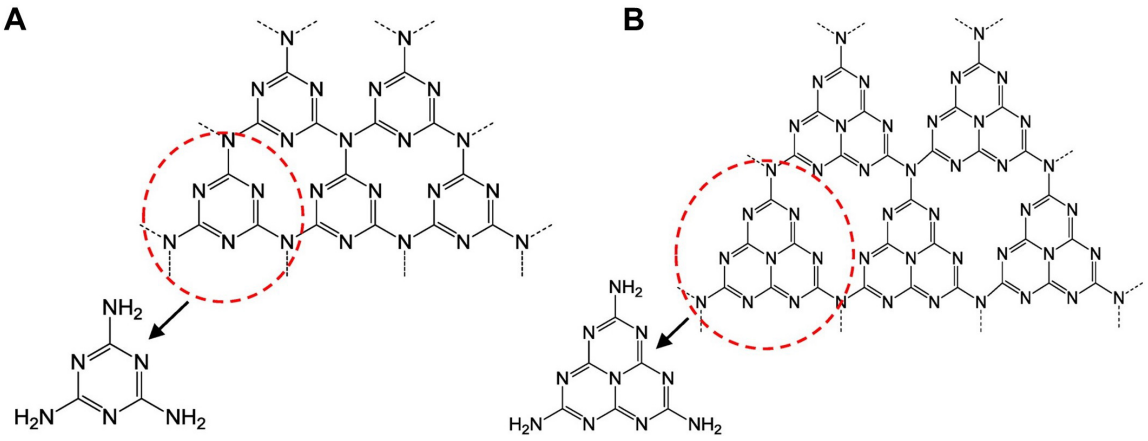

Figure 4. (A) Triazine and (B) tri-*s*-triazine (heptazine) structures of graphitic carbon nitride (g-C_3N_4). Reproduced from Ref.[30] with permission from the American Chemical Society.

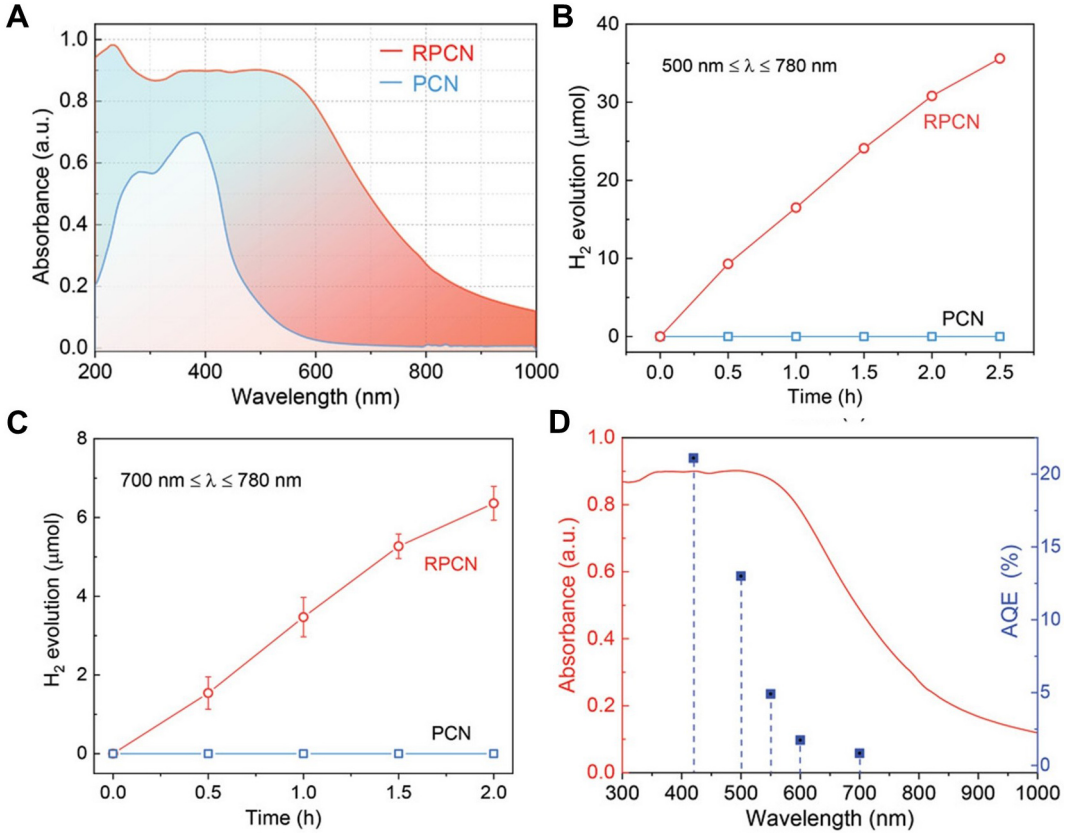

Figure 5. (A) Ultraviolet-Visible-Near Infrared (UV-Vis-NIR) diffuse reflection spectra. Activity of H_2 production from water with RPCN under irradiation within different light ranges of (B) 500 ≤ λ ≤ 780 nm and (C) 700 ≤ λ ≤ 780 nm, using ~3 wt.% Pt as the cocatalyst and 10 vol.% TEOA as the sacrificial agent. (D) AQE at various monochromatic wavelengths. Reproduced from Ref.[37] with permission from Wiley. RPCN: Polymeric carbon nitride; TEOA: triethanolamine; AQE: apparent quantum efficiency.

IV. Metal-organic framework-based photocatalysts

Metal-organic frameworks (MOFs) are porous materials self-assembled from inorganic metal oxide clusters and organic linkers[38-40]. Owing to their unique properties that include high surface areas, well-defined metal

nodes, adjustable chemical composition and enriched functionality, they have been extensively applied in various fields, such as gas separation and storage, sensors, environmental purification and catalysis[3,38,41,42].

In 2018, Xiao *et al.*[43] combined surface plasmonic Au with a Pt-MOF Schottky junction to synthesize a Pt@MIL-125/Au catalyst [MIL-125 is a Ti-based MOF consisting of $Ti_8O_8(OH)_4$ clusters and terephthalate acid linkers]. The spatial separation of the Pt and Au particles steered the formation of electron flow and expedited electron transport. Therefore, Pt@MIL-125/Au showed a much higher photocatalytic H_2 production rate compared to catalysts with Pt or Au from water under the illumination of visible light with TEOA as electron donors.

Chen *et al.*[39] bestowed the organic linkers (2-aminoterephthalate acid) of NH_2-MIL-125(Ti) with mixed-valent copper (Cu^{2+}/Cu^{+}) centers (Cu-NM), which enabled effective electron transfer to the mixed-valent Cu^{2+}/Cu^{+} centers from the 2-aminoterephthalate acid linkers [Figure 6A and B]. This resulted in increases in the carrier density and lifetime of the photogenerated charges by 7000 and 27 times, respectively. As a result, a much higher rate of H_2 production compared to that of MOFs with Pt as a cocatalyst (Pt-NM) was obtained under the illumination of visible light from water when TEA was used as a sacrificial hole scavenger [Figure 6C].

Dong *et al.*[44] fabricated a CdS-based MOF, DLNU-M-CdS(H_2TD) (H_2TD = 1,3,4-thiadiazole-2,5-dithiol), for photocatalytic H_2 production in the presence of TEOA without the assistance of cocatalysts. During the photocatalytic reaction, the electron-donating process from TEOA to H_2TD evoked fast electron transfer in the path of TEOA→H_2TD→Cd→H^+ to separate photogenerated e^--h^+ pairs in DLNU-M-Cd(H_2TD), resulting in a H_2 production rate of 26.1 mmol·g^{-1}·h^{-1} under the irradiation of UV-visible-light.

Sun *et al.*[45] incorporated noble-metal-free Ni_2P and $Ni_{12}P_5$ into UiO-66-NH_2 [a MOF consisting of $Zr_6O_6(OH)_4$ clusters and 2-aminoterephthalate acid linkers] to form Ni_2P@MOF and $Ni_{12}P_5$@MOF photocatalysts, respectively, for photocatalytic H_2 production with TEA as a hole sacrificial agent. Both Ni_2P@MOF and $Ni_{12}P_5$@MOF showed enhanced H_2 production rates in comparison with the pristine MOF and their physical mixtures. Ni_2P and $Ni_{12}P_5$ exhibit a similar capability to Pt in promoting the charge transfer from linkers to clusters and lowering the activation energy of the H_2 production reaction. Pt is thermodynamically favorable, while Ni_2P is kinetically more suitable for H_2 production, resulting in higher activity over Ni_2P@MOF than over Pt@MOF.

Meng *et al.*[46] immobilized CdS quantum dots and carbon nanodots (CDs) in the cages of MIL-101 (a Cr-based MOF consisting of Cr clusters and terephthalic acid linkers) to form CD/CdS@MIL-101 composites. The H_2 production rate on CD/CdS@MIL-101 with a CD content of 5.2 wt.% was 14.66 μmol·h^{-1} when using lactic acid as a sacrificial agent under the illumination of visible light, which was 8.5 and 18.6 times that on CdS@MIL-101 and pure CdS, respectively. The enhanced photoactivity can be ascribed to the role of electron collection of the CDs, which prolongs the lifetime of the photogenerated charge carriers in the CdS@MIL-101 heterostructure photocatalyst.

Lin *et al.*[47] demonstrated porphyrin-based zirconium MOFs (PCN-H_2/$Pt_{x:y}$, x:y = 4:1, 3:2, 2:3 and 0:1) with different ratios of H_2TCPP and Pt^{II}TCPP [TCPP = tetrakis(4-carboxyphenyl)porphyrinate] linkers. PCN-H_2/$Pt_{0:1}$ displayed the highest H_2 production reaction rate (351.08 μmol·h^{-1}·g^{-1}) with TEOA as a sacrificial agent under visible-light irradiation. Such photoactivity can be ascribed to the uniformly dispersed Pt^{2+} ions in PCN-H_2/$Pt_{0:1}$, which boost the transfer of charges from porphyrins (photosensitizers) to Pt^{II} ions (catalytic centers).

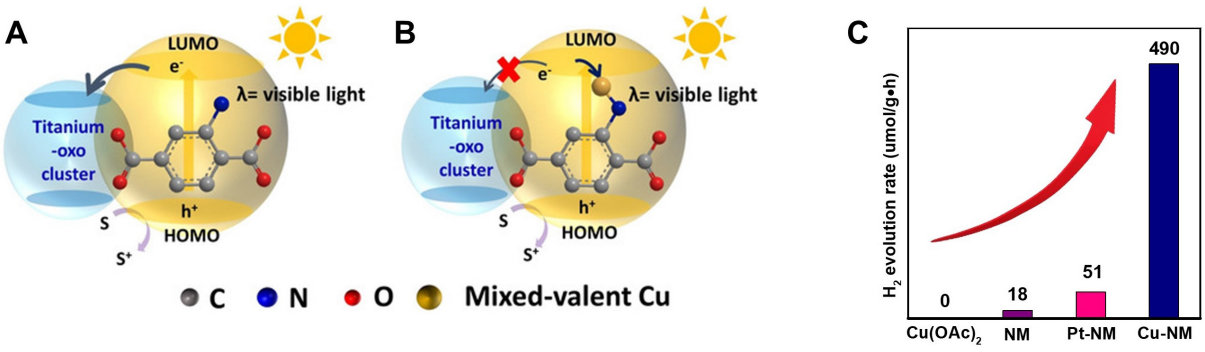

Figure 6. (A) and (B) Schematic of electron-transfer pathways from an organic linker to a titanium-oxo cluster in NH_2-MIL-125(Ti) and to a mixed-valent Cu center, respectively. S represents a sacrificial agent. (C) Activity of NM, Pt-NM and Cu-NM in photocatalytic H_2 production under visible-light irradiation. Reproduced from Ref.[39] with permission from Wiley.

V. Covalent-organic framework-based photocatalysts

Covalent-organic frameworks (COFs) are another type of porous crystalline polymers that can precisely integrate molecular building blocks into extended 2D or three-dimensional (3D) structures via covalent bonds[48-50]. Because of their characteristics, which include low density, high porosity, structural periodicity and modular functionality, COFs have been extensively studied for gas adsorption and separation[51,52], catalysis[53,54], sensors[55-57], optoelectronics[58,59] and energy storage systems[60-62].

In 2018, Xie *et al.*[63] reported a highly ordered COF, CTF-1 ($C_8N_2H_4$), which can efficiently produce H_2 from water. A high AQE for H_2 production of 6% at λ = 420 nm was obtained, which was ascribed to the well-defined and ordered structure of CTF-1, as well as low carbonization and superior band positions. In 2021, Chen *et al.*[64] reported the synthesis of four isostructural porphyrinic 2D COFs (*M*Por-DETH-COF, *M* = H_2, Co, Ni, Zn; DETH = 2,5-diethoxyterephthalohydrazide) and their application in photocatalytic H_2 production [Figure 7]. All four COFs have AA stacking structures with high crystallinity and large surface areas. The introduction of different transition metals into the porphyrin rings regulated the photocatalytic H_2 production rate of these COFs in the following order: CoPor-DETH-COF < H_2Por-DETH-COF < NiPor-DETH-COF < ZnPor-DETH-COF. In the same year, COFs with an ordered arrangement of layered structures were reported for visible-light-driven H_2 production with ascorbic acid as a sacrificial agent[65]. The mesoporous channels of a β-ketoenamine-linked COF, including a benzothiadiazole moiety, were filled with polyethylene glycol, which inhibited the dislocation of neighboring layers while retaining the columnar π-orbital arrays to boost free charge transfer. Thus, the H_2 production rate was enhanced compared to that of the pure COFs. Yang *et al.*[66] demonstrated that donor-acceptor-type imine-linked COFs could catalyze H_2 production with a rate of 20.7 $mmol \cdot g^{-1} \cdot h^{-1}$ under the illumination of visible light with ascorbic acids as hole scavengers. The improved photoactivity was ascribed to the extended light harvesting range, enhanced charge separation efficiency and increased hydrophilicity.

VI. Nitride-based photocatalysts

Nitrides, particularly transition metal nitrides with narrow energy bandgaps and excellent physicochemical properties, can effectively regulate the structures of semiconductor photocatalysts and their photocatalytic performance[67].

In 2021, Xiao *et al.*[68] fabricated Mg-Zr-codoped single-crystalline Ta_3N_5 (Ta_3N_5:Mg+Zr) nanoparticles for H_2 production from H_2O. The photoactivity was 45 times that of pristine Ta_3N_5. Simultaneous defect tuning and surface property optimization generated high concentrations of long-lived electrons and facilitated

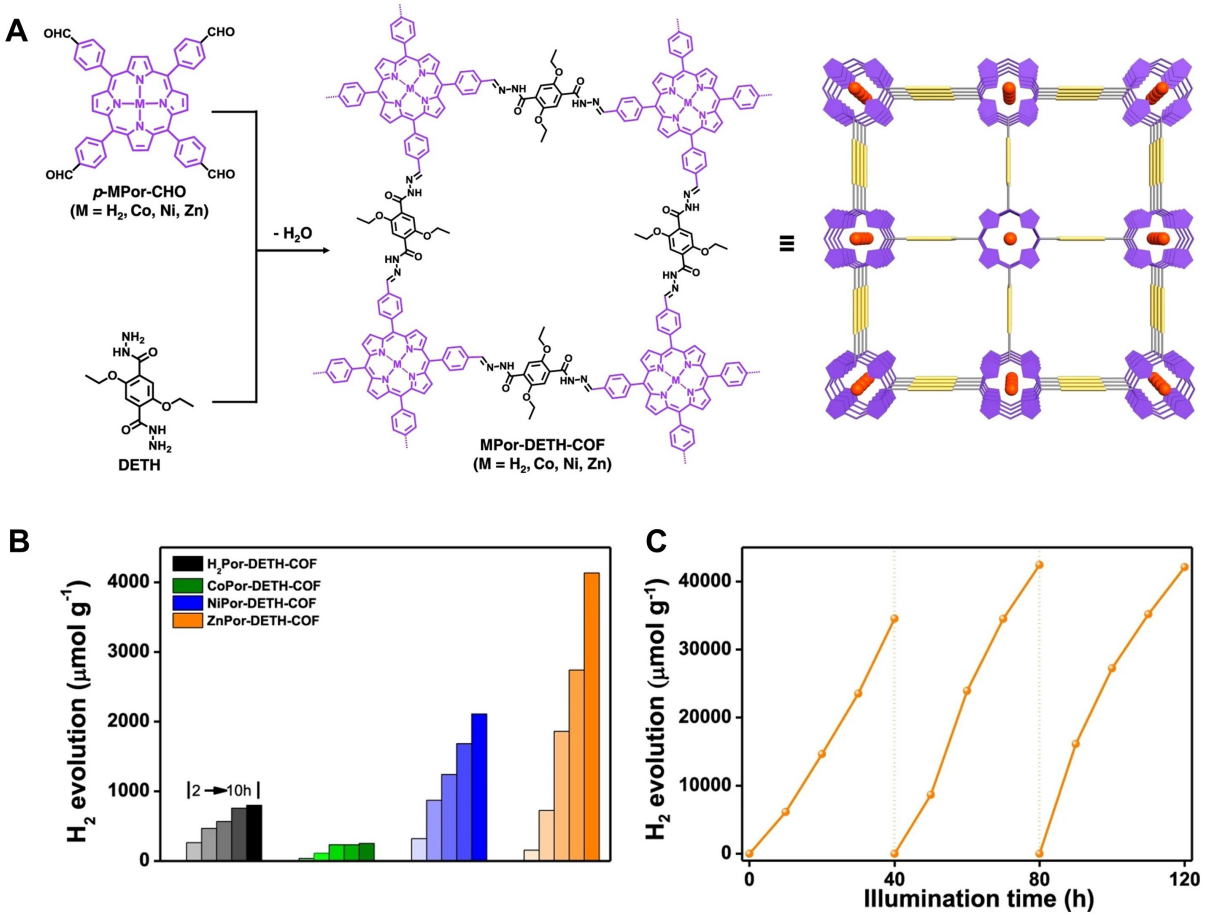

Figure 7. (A) Schematic illustration of the synthesis of *M*Por-DETH-COFs. (B) Activity of H_2 production under visible-light irradiation using H_2Por-DETH-COF, CoPor-DETH-COF, NiPor-DETH-COF and ZnPor-DETH-COF. (C) Cycling results of H_2 production under visible-light irradiation using ZnPor-DETH-COF. Reproduced from Ref.[64] with permission from Springer Nature.

electron migration to the Pt sites on the surface of the photocatalyst, thus enhancing the photoactivity under the illumination of visible light. In the same year, Wang *et al.*[69] reported the efficient utilization of photogenerated electrons in a single-crystal $BaTaO_2N$ photocatalyst for H_2 production via the sequential decoration of a Pt cocatalyst. The H_2 production rate in a methanol aqueous solution was improved 100-fold compared to that of $BaTaO_2N$. Its AQE was 6.8% at λ = 420 nm.

H_2 production from overall water splitting

Photocatalytic H_2 production from overall water splitting can effectively avoid the secondary pollution caused by the use of sacrificial hole scavengers, while O_2 is produced from water oxidation.

I. Selenide- and sulfide-based photocatalysts

Wang *et al.*[70] developed uniform hollow $MoSe_2$/CdSe nanospheres without any template/surfactant assistance. Owing to the Z-scheme mechanism for charge transfer in the heterostructure, it displayed a H_2 production rate of 7120.0 $\mu mol \cdot g^{-1} \cdot h^{-1}$ from water splitting under the irradiation of simulated sunlight and the AQE reached 27.2% at λ = 670 nm.

S 3p and O 2p orbitals were hybridized by Zhang *et al.*[71] to generate oxysulfides with stabilization of S^{2-} in a sulfide-based photocatalyst. Additional surface modification of the oxysulfides with dual cocatalysts promoted the separation and transfer of photogenerated charges, thereby reducing charge accumulation and inhibiting photocorrosion. The results demonstrated that the pH value played an important role in realizing the efficient production of stoichiometric H_2 and O_2. Pan *et al.*[72] reported that Ag dopant and nanohole dual defects in $ZnIn_2S_4$ monolayers promoted stoichiometric H_2 and O_2 production from water under the illumination of visible light. The Ag dopant and nanohole dual defects optimized the light harvesting and carrier dynamics and served as active sites for the oxidation and reduction of water, respectively, thereby resulting in stable activity for photocatalytic water splitting.

II. C_3N_4-based photocatalysts

Chen *et al.*[73] constructed 3D porous g-C_3N_4 assembled using highly crystalline and ultrathin NSs. The 3D g-C_3N_4 NSs could produce H_2 and O_2 from water splitting with production rates of 101.4 and 49.1 μmol·g^{-1}·h^{-1}, respectively, under the illumination of visible light. These rates are ~11.8 and ~5.1 times that of bulk g-C_3N_4 and g-C_3N_4 NSs, respectively. Furthermore, the 3D g-C_3N_4 NSs showed an AQE of 1.4% under light radiation at λ = 420 nm and maintained good stability for 100 h. Lin *et al.*[74] demonstrated a one-photon excitation route by coupling a polymeric carbon nitride (PCN) with LaOCl to realize overall water splitting. The modification of LaOCl formed an interfacial electric field that boosted the rapid separation and transfer of photogenerated e^--h^+ pairs in the catalyst. The water reduction half-reaction occurred on LaOCl and its oxidation half-reaction appeared on the PCN. As a result, this "artificial photosynthesis" catalyst showed H_2 and O_2 production rates of 22.3 and 10.7 μmol·h^{-1}, respectively, from overall water splitting.

Chen *et al.*[75] synthesized a g-C_3N_4/reduced graphene oxide (rGO)/perylene diimide polymer (PDIP) photocatalyst with a Z-scheme heterostructure to achieve excellent photocatalytic overall water splitting [Figure 8A]. A significant internal electric field was built in the Z-scheme heterostructure [Figure 8B], thereby promoting the high-flux charge transfer and improving the charge separation efficiency by a factor of 8.5. The g-C_3N_4/rGO/PDIP photocatalyst presented H_2 and O_2 production rates of 15.80 and 7.80 μmol·h^{-1}, respectively, which are ~12.1 times that of pure g-C_3N_4. An AQE of 4.94% at λ = 420 nm and a conversion efficiency of solar energy to hydrogen energy of 0.3% were realized [Figure 8C and D]. Besides, it showed a very good stability within 120 h of photocatalytic reaction [Figure 8E].

Wu *et al.*[76] prepared g-C_3N_4 NSs exfoliated by a femtosecond pulsed laser, which achieved H_2 and O_2 production rates of 42.6 and 18.7 μmol·g^{-1}·h^{-1}, respectively, toward overall water splitting when Pt was used as a cocatalyst. The laser pulses created cyano (-C≡N) defects that favored the anchoring of divalent atomic Pt cocatalysts, which are different from Pt metal nanoparticles. This provided more active sites for the surface reaction and suppressed the reverse reaction of water splitting. In addition, the -C≡N defects reduced the position of the band edge to improve the oxidation ability of h^+.

Using an electrostatic self-assembly method, Zhao *et al.*[77] coupled B-doped N-deficient 2D C_3N_4 NSs to obtain a 2D/2D polymeric Z-scheme heterostructure. The combination of ultrathin nanostructures, the robust interfacial interaction and the staggered band arrangement in the Z-scheme system boosted the separation and transfer of photogenerated e^--h^+ pairs, thus realizing stoichiometric H_2 and O_2 production from photocatalytic overall water splitting with Pt and $Co(OH)_2$ cocatalysts.

III. MOF-based photocatalysts

In 2020, a Pt@UiO-66-NH_2@MnO_x photocatalyst with Pt and MnO_x cocatalysts was designed by

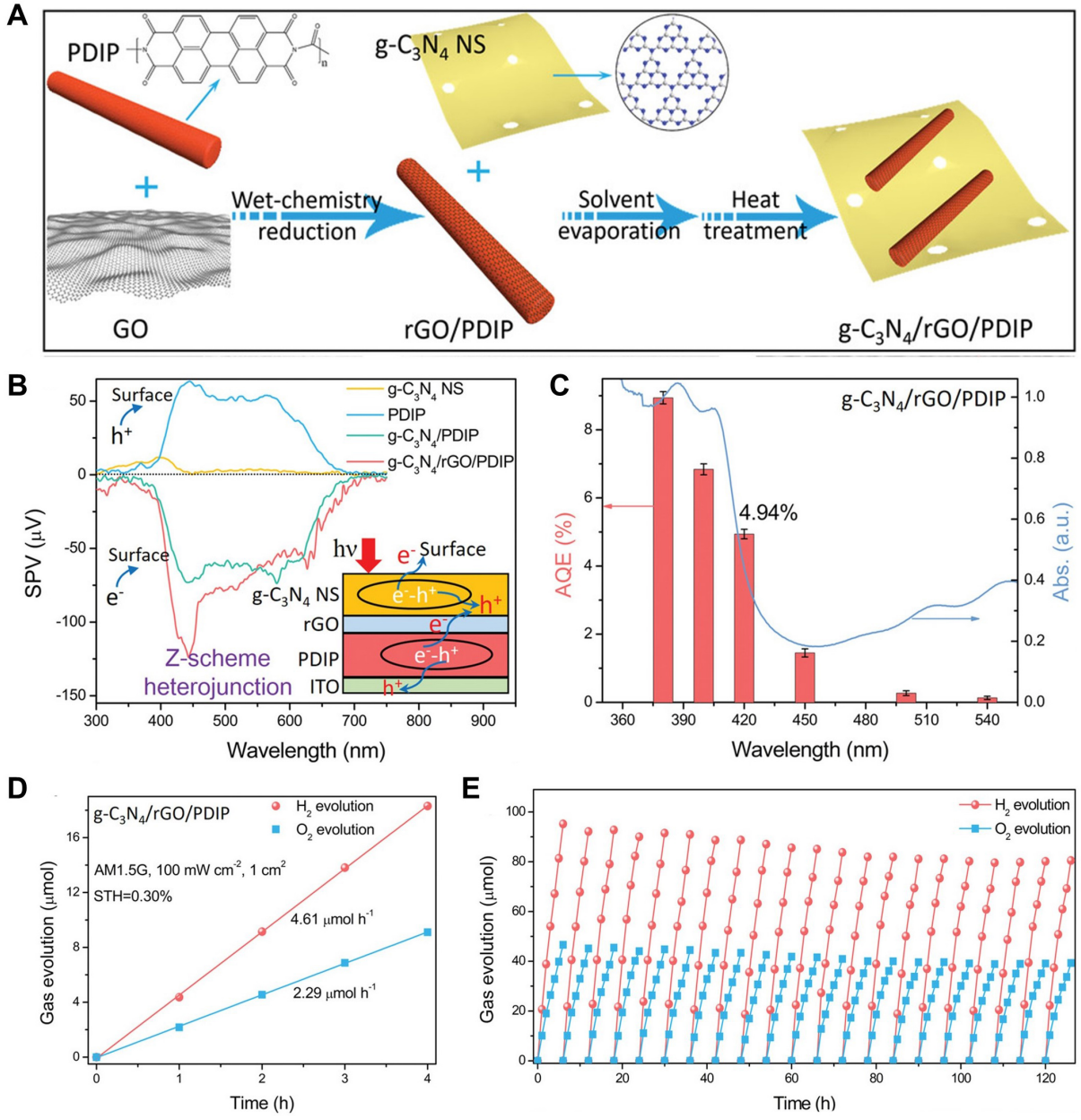

Figure 8. (A) Schematic illustration of g-C_3N_4/rGO/PDIP fabrication. (B) Surface photovoltage (SPV) spectra. (C) Wavelength dependency of AQE for photocatalytic overall water splitting. (D) Photocatalytic activity of overall water splitting under AM 1.5G simulated sunlight irradiation using g-C_3N_4/rGO/PDIP. (E) Cycling results of photocatalytic overall water splitting. Reproduced from Ref.[75] with permission from Wiley. rGO: Reduced graphene oxide; PDIP: perylene diimide polymer.

Zhang *et al.*[78] for the complete spatial separation of photogenerated e^--h^+ pairs in UiO-66-NH_2, thereby realizing H_2 and O_2 production from water. Compared with UiO-66-NH_2, Pt@UiO-66-NH_2 and UiO-66-NH_2@MnO_x photocatalysts, Pt@UiO-66-NH_2@MnO_x exhibited the highest photoactivity for overall water splitting. As cocatalysts, Pt favored the trapping of photogenerated e^-, while MnO_x particles tended to collect photogenerated h^+. The photogenerated e^- and h^+ flowed to the inside and outside of the MOF, respectively, accumulating on the respective cocatalysts and further inducing redox reactions.

Significantly, Hu *et al.*[79] integrated a H_2 evolution reaction (HER)-MOF and a water oxidation reaction (WOR)-MOF into liposomal structures for the spatial separation of photogenerated e^--h^+ pairs. The HER-MOF consisted of a light-harvesting Zn-porphyrin and a catalytic Pt-porphyrin and was modified with pentafluoropropionic acid, making the HER-MOF hydrophobic and thus promoting its binding to the hydrophobic lipid bilayer of the liposome. The WOR-MOF was composed of a $[Ru(2,2'\text{-bipyridine})_3]^{2+}$-based photosensitizer and an Ir-bipyridine catalytic center and was localized in the hydrophilic interior of the liposome. Owing to the rapid electron transfer from the Zn-porphyrin and $[Ru(2,2'\text{-bipyridine})_3]^{2+}$ antennae to the Pt-porphyrin and Ir-bipyridine reaction centers and the efficient charge separation in the lipid bilayers, this liposome-MOF achieved H_2 and O_2 production in a ~2:1 ratio with an AQE of ~1.5%.

IV. Other photocatalysts

Wang *et al.*[80] reported quadruple-band InGaN NW arrays, which are composed of $In_{0.35}Ga_{0.65}N$, $In_{0.27}Ga_{0.73}N$, $In_{0.20}Ga_{0.80}N$ and GaN sections, with energy bandgaps of 2.1, 2.4, 2.6, and 3.4 eV, respectively. These multiband InGaN NW arrays were modified upon a nonplanar wafer to improve the light absorption. The doping gradient was introduced along the NWs to form a built-in electric field, which separated and extracted photogenerated charge carriers for water redox reactions. This InGaN photocatalyst exhibited a solar-to-hydrogen efficiency of ~5.2%.

Pan *et al.*[81] used rGO NSs to promote the transfer of photogenerated charge carriers between H_2 producing photocatalysts (e.g., carbon nitride and $BiVO_4$) and O_2 evolution photocatalysts (e.g., Fe_2O_3 and WO_3), thereby realizing efficient overall water splitting. Furthermore, Oshima *et al.*[82] presented $HCa_2Nb_3O_{10}$ NSs sensitized by a Ru(II) tris-diimine photosensitizer for overall water splitting under visible-light irradiation, combined with a WO_3-based water oxidation photocatalyst and a I_3^-/I^- redox couple. The Pt-intercalated $HCa_2Nb_3O_{10}$ NSs, which were further modified with amorphous Al_2O_3 clusters as H_2 production components, realized a dye-based turnover number and frequency of 4580 and 1960 h^{-1}, respectively. Its AQE at 420 nm was 2.4%.

Zhao *et al.*[83] presented a practically feasible strategy that mimicked natural photosynthesis known as the hydrogen farm project (HFP). The proposed system comprised solar energy harvesting and H_2 production subsystems integrated by a Fe^{3+}/Fe^{2+} redox ion pair [Figure 9]. The $BiVO_4$ crystals with accurately tuned {110}/{010} facets were used as photocatalysts for this project. The AQE of photocatalytic water oxidation and the complete forward reaction is 71% and there is almost no reverse reaction. A solar-to-chemical conversion efficiency of > 1.9% was also achieved.

In 2020, Takata *et al.*[84] used an aluminum-doped strontium titanate ($SrTiO_3$:Al) photocatalyst to realize an AQE of 96% for overall water splitting at wavelengths of 350-360 nm, which was equivalent to an almost uniform internal quantum efficient. The selective photodeposition of Rh/Cr_2O_3 and CoOOH cocatalysts upon different crystal facets of the photocatalyst for the $H_2$and O_2 production reactions, respectively, boosted the H_2 and O_2 production reactions separately. Thus, multiple consecutive forward charge transfers without reverse charge transfer were realized, thereby attaining the maximum AQE for overall water splitting.

Photocatalytic H_2 production from hydrogen storage materials

Achieving the efficient storage and transportation of gaseous H_2 is a significant challenge. Storing H_2 in a liquid or solid material that holds H_2 under ambient conditions and releases it as the conditions change is a safe and efficient method[3]. In particular, many efforts have been made to achieve the release of H_2 from H_2 storage materials, such as ammonia borane (AB) and formic acid (FA).

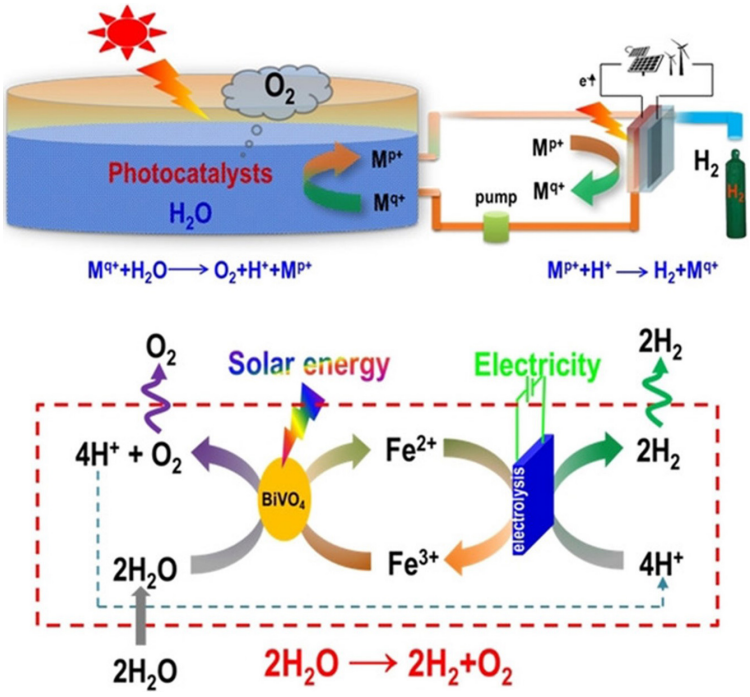

Figure 9. (A) Schematic of hydrogen farm project (HFP) for scalable solar H_2 production using particulate photocatalysts for water oxidation and a shuttle ion loop for energy storage. (B) Practical realization for HFP using $BiVO_4$ as a water oxidation photocatalyst, Fe^{3+}/Fe^{2+} as shuttle ions for energy storage and an electrolysis cell for H_2 production. Reproduced from Ref.[83] with permission from Wiley.

In 2018, Zhang *et al.*[85] demonstrated the NIR-plasmonic energy up-conversion process in Yb^{3+}/Er^{3+}-doped $NaYF_4$ nanoparticle ($NaYF_4$:Yb-Er NP)@$W_{18}O_{49}$ NW heterostructures. The improvement of the up-conversion luminescence of the $NaYF_4$:Yb-Er NPs was attributed to the NIR-excited localized surface plasmon resonance (LSPR) of the $W_{18}O_{49}$ NWs. Simultaneously, this plasmon-enhanced up-conversion luminescence was partly absorbed by the $W_{18}O_{49}$ NWs, re-exciting its higher energy LSPR [Figure 10A]. Based on this plasmonic energy transfer process, the $NaYF_4$:Yb-Er NP@$W_{18}O_{49}$ NW heterostructures exhibited an ~35-fold increase in catalytic H_2 production from AB [Figure 10B and C].

Very recently, Zhang *et al.*[86] reported a Pd-decorated Ti-MOF@TpTt composite (Pd@Ti-MOF@TpTt) coated with an ultrathin COF nanobelt [Figure 11A]. This catalyst presented much higher photoactivity for H_2 production from AB hydrolysis than that of the other counterparts with fibrillar-like COF shells [Figure 11B]. This improved activity could be ascribed to its high surface area, core-shell structure and type II heterojunction [Figure 11C], which provided more active sites and promoted the separation of photogenerated e^--h^+ pairs. Finally, Pd@Ti-MOF@TpTt displayed excellent stability for H_2 production [Figure 11D].

Cao *et al.*[87] synthesized a CdS/CoP@rGO hybrid for photocatalytic H_2 production from FA using ultrasmall CoP nanoparticles as a cocatalyst for the first time. The visible-light-driven H_2 production rate using the CdS/CoP@rGO hybrid reached 182 ± 12.5 $\mu mol \cdot mg^{-1} \cdot h^{-1}$ without any additives, which was 30 times that of the bare CdS. The system could be sustained for more than seven days.

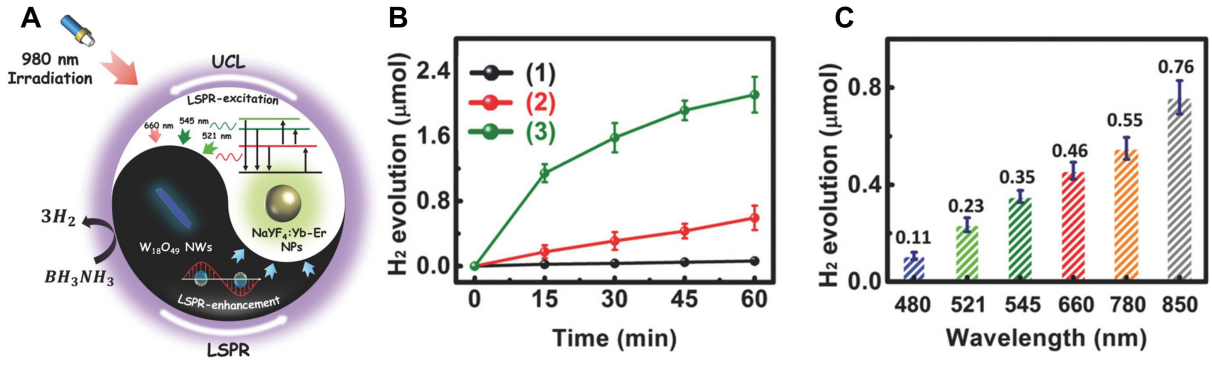

Figure 10. (A) Schematic diagram of plasmonic energy upconversion in the $NaYF_4$:Yb-Er NP/$W_{18}O_{49}$ NW heterostructure system upon irradiation at λ = 980 nm. (B) Amount of H_2 production from AB aqueous solution under irradiation at λ = 980 nm: (1) no catalyst; (2) $W_{18}O_{49}$ NWs; and (3) $NaYF_4$:Yb-Er NW@$W_{18}O_{49}$ NP heterostructures. (C) Amount of H_2 production of $W_{18}O_{49}$ NWs in 1 h under irradiation at different incident light wavelengths. Reproduced from Ref.[85] with permission from Wiley.

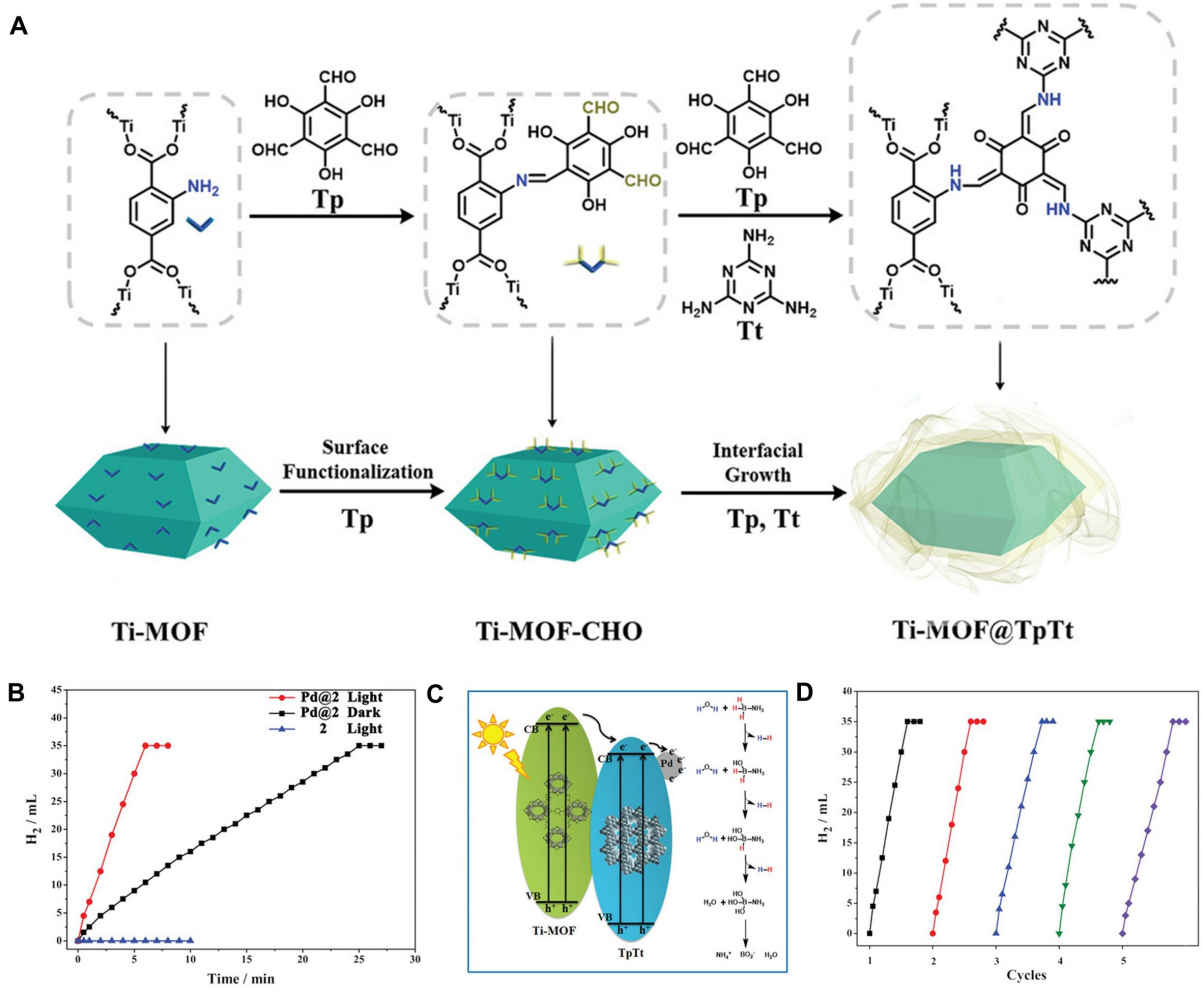

Figure 11. (A) Schematic illustration of the synthesis of Pd-decorated Ti-MOF@TpTt hybrids. (B) Activity of H_2 production from AB aqueous solution over Pd@Ti-MOF@TpTt and Ti-MOF@TpTt under different conditions. (C) Proposed mechanism for AB hydrolysis catalyzed by Pd@Ti-MOF@TpTt. (D) Cycling results of AB hydrolysis under light irradiation using Pd@Ti-MOF@TpTt. Reproduced from Ref.[86] with permission from Wiley.

Zhang *et al.*[88] loaded AuPd nanoparticles upon super-small carbon nitride nanospheres (AuPd/CNS) to construct a Mott-Schottky photocatalyst and used it to catalyze H_2 production from FA. It showed a turnover frequency of 1017.8 h^{-1} under visible-light illumination ($\lambda > 420$ nm). The alloying, plasmonic and Mott-Schottky effects optimized the electronic structure of Pd in the AuPd/CNS composite, which accelerated the electrons transferred from the carbon nitride and Au to the active Pd sites, thus resulting in improved photoactivity.

Photocatalytic CO_2 conversion

Basic principles of photocatalytic CO_2 conversion

The overuse of fossil resources has led to excessive CO_2 emissions, which have contributed to the greenhouse effect. There are already many technologies for collecting and sequestering CO_2, such as scrubbing, mineral carbonation, geological injection and oceanic injection[89]. Nevertheless, these technologies are expensive and may cause the leakage of CO_2[89,90]. Alternatively, CO_2 can be considered as a low-cost, safe and abundant carbon source that can be converted into valuable energy fuels. This strategy could not only reduce CO_2 emissions and alleviate the greenhouse effect, but also mitigate the energy crisis.

CO_2 is highly thermodynamically stable and its C=O bond energy (750 kJ·mol^{-1}) is much larger than that of C-H (411 kJ·mol^{-1}), C-O (327 kJ·mol^{-1}), and C-C (336 kJ·mol^{-1}) single bonds[91,92]. Thus, the photocatalytic conversion of CO_2 to hydrocarbons requires high energy input to activate the C=O double bonds and convert them into C-H single bonds. Photogenerated e^- with an appropriate reduction potential can supply a driving force for the reduction of CO_2. Photocatalytic CO_2 conversion takes place through a multi-step reaction pathway with the participation of 2, 6, 8, 12, 14 or 18 e^- and H^+ [Figure 12][93,94]. Various products, including C_1 compounds (e.g., CO, CH_4, HCOOH, CH_3OH and HCHO) and C_2 molecules (e.g., CH_2CH_2, C_2H_5OH and CH_3COOH)[95], can be generated. Some reactions related to photocatalytic CO_2 conversion and the relevant reduction potentials (E^0) are listed in Table 1[96,97].

As shown in Table 1, a reduction potential of -1.85 V is required for direct single-electron CO_2 reduction[98]. So far, almost no photocatalysts have displayed sufficient ability to drive this single-electron transfer process. On the contrary, H^+-assisted multi-electron/H^+ reduction represents an alternative and more advantageous method.

Recent advances in photocatalytic CO_2 conversion

Photocatalytic CO_2 conversion with H_2O

The utilization of H_2O as a reducing agent to photocatalytically convert CO_2 is an intriguing process[99] that involves multi-electron reactions [Table 1][100,101]. As a result, various products, such as CO[102,103], CH_4 and CH_3OH, can be obtained. Taking CO production as an example, the photogenerated h^+ oxidize H_2O into O_2 with the generation of H^+ (Equation 5), while the photogenerated e^- reduce CO_2 to CH_4 via a two-electron reaction with two protons (Equation 6):

$$H_2O + 2h^+ \rightarrow 1/2O_2 + 2H^+ (5)$$

$$CO_2 + 2H^+ + 2e^- \rightarrow CO + H_2O (6)$$

At present, photocatalytic CO_2 conversion with H_2O mainly involves two reaction systems[89]. One is a liquid phase system, in which the CO_2 conversion efficiency is largely limited due to the low solubility of CO_2 (~0.03 M under ambient conditions) with the occurrence of competitive H_2 production from H_2O. Thus, many efforts have been made to enhance the pressure of CO_2 and increase the solubility of CO_2 in alkaline

Table 1. Electrochemical reactions involved in aqueous CO_2 and proton reduction with their corresponding reduction potentials E^0 (V *vs.* NHE at pH 7)

Entry	Equation	Product	E^0 (V)
1	$CO_2 + e^- \rightarrow CO_2^-$	Carbonate anion radical	-1.85
2	$CO_2 + 2H^+ + 2e^- \rightarrow HCOOH$	Formic acid	-0.61
3	$CO_2 + 2H^+ + 2e^- \rightarrow CO + H_2O$	Carbon monoxide	-0.53
4	$CO_2 + 4H^+ + 4e^- \rightarrow HCHO + H_2O$	Formaldehyde	-0.48
5	$CO_2 + 4H^+ + 4e^- \rightarrow C + 2H_2O$	Carbon	-0.20
6	$CO_2 + 6H^+ + 6e^- \rightarrow CH_3OH + H_2O$	Methanol	-0.38
7	$CO_2 + 8H^+ + 8e^- \rightarrow CH_4 + 2H_2O$	Methane	-0.24
8	$2CO_2 + 12H^+ + 12e^- \rightarrow C_2H_4 + 4H_2O$	Ethylene	-0.34
9	$2CO_2 + 12H^+ + 12e^- \rightarrow C_2H_5OH + 3H_2O$	Ethanol	-0.33
10	$2CO_2 + 14H^+ + 14e^- \rightarrow C_2H_6 + 4H_2O$	Ethane	-0.27
11	$3CO_2 + 18H^+ + 18e^- \rightarrow C_3H_7OH + 5H_2O$	Propanol	-0.32
12	$2H^+ + 2e^- \rightarrow H_2$	Hydrogen	-0.42

Reproduced from Ref.[96] with permission from Wiley.

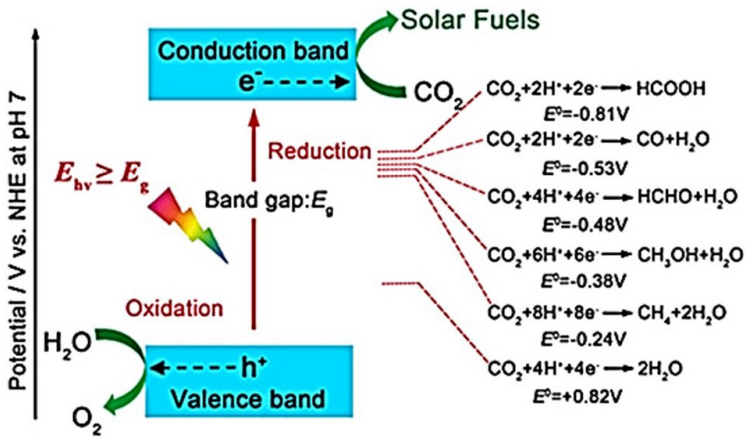

Figure 12. Schematic energy diagram for CO_2 reduction and H_2O oxidation on a semiconductor. Reproduced from Refs.[93,94] with permission from Wiley.

systems[104]. The other is a gas-phase system that uses CO_2 and H_2O vapor and realizes a higher selectivity for CO_2 reduction[105]. Multifarious photocatalysts have been explored for CO_2 conversion using H_2O.

I. Metal oxide-based photocatalysts

Sorcar *et al.*[106] reported bimetallic Cu-Pt nanoparticle-sensitized blue titania (TiO_2) that generated large amounts of CH_4 and CH_3CH_3 during artificial-sunlight-driven CO_2 reduction with H_2O. Within 6 h of the reaction, 3.0 mmol·g^{-1} of CH_4 and 0.15 mmol·g^{-1} of CH_3CH_3 were produced.

Li *et al.*[107] reported a cake-like porous TiO_2 photocatalyst with the surface-localized doping of copper and cobalt. The doped TiO_2 photocatalyst boosted the photoreduction of CO_2 with water vapor. 1% Cu-doped TiO_2 promoted the breaking of C=O bonds. The production rates of CO and CH_4 reached 45.31 and 42.35 μmol·h^{-1}, respectively, under simulated sunlight irradiation. This activity was further enhanced by incorporating trace cobalt. In addition to the enhanced performance in terms of the production of CO and CH_4, the selectivity was also increased for the production of hydrocarbons (C_{2+}). The production rates of

C_2H_6 and C_3H_8 reached 89.20 and 3.36 μmol·h^{-1}, respectively, over 0.02% Co-1% Cu/TiO_2. The incorporation of copper and cobalt ions realized efficient charge separation in the catalyst, resulting in the generation and enrichment of methyl radicals upon cobalt ions, which induced the production of C_{2+}.

Atomically dispersed Cu-supported mesoporous TiO_2 ($mTiO_2$) was used for the light-driven reduction of CO_2 with H_2O by Yuan *et al.*[108]. The authors revealed that the atom-dispersed Cu(II) underwent reduction to Cu(I) and finally to Cu(0), with the mixture of Cu(I) and Cu(0) proving effective for the production of CH_4.

La- and Rh-doped $SrTiO_3$ ($SrTiO_3$:La,Rh) and Mo-doped $BiVO_4$ ($BiVO_4$:Mo) light absorbers were integrated into a photocatalyst by Wang *et al.*[109]. This photocatalyst converted CO_2 and H_2O into formate ($HCOO^-$) and O_2 and achieved a solar-to-$HCOO^-$ conversion efficiency of 0.08% and a selectivity of 97%.

Z-scheme type photocatalysts composed of g-C_3N_4 and Au-loaded anatase TiO_2 (A-TiO_2) were fabricated by Wang *et al.*[110]. The surface heterojunction between the coexposed {001} and {101} facets in A-TiO_2 improved the separation efficiency of the photogenerated e^--h^+ pairs. The loaded Au gathered and transferred the stimulated electrons originating from A-TiO_2 to g-C_3N_4. The g-C_3N_4 component trapped the photogenerated e^- and improved the adsorption ability of CO_2. This catalyst exhibited high photoactivity of CO_2 conversion under the illumination of visible light, with CH_4 and CO formation rates of 37.4 and 21.7 μmol·g^{-1}·h^{-1}, respectively.

Wang *et al.*[111] loaded Ag and Co dual cocatalysts on Al-doped $SrTiO_3$ [Figure 13], which brought about an enhanced CO production rate and a corresponding selectivity of 99.8% at λ = 300 nm. The CO production rate of 52.7 μmol·h^{-1} was 12 times that of the catalyst without Co cocatalysts (4.7 μmol·h^{-1}). The AQE for CO production was ~0.03% at λ = 365 nm, with a selectivity of 98.6% for CO production. The Ag and Co cocatalysts acted as reduction and oxidation sites to promote the production of CO and O_2, respectively.

A CuO_x@p-ZnO photocatalyst with CuO_x uniformly dispersed on polycrystalline ZnO was fabricated by Wang *et al.*[112]. This catalyst reduced CO_2 to C_2H_4 with a selectivity of 32.9% and the production rate was 2.7 μmol·g^{-1}·h^{-1} with H_2O as a hole scavenger under illumination. During the reduction reaction, a unique Cu^+ site was formed on the surface of the CuO matrix and this surface Cu^+ site can anchor the generated CO and further stabilize the intermediate *OC-COH of C-C coupling, which thus promoted the production of C_2H_4.

II. MOF- and COF-based photocatalysts

Lu *et al.*[113] synthesized crystalline porphyrin tetrathiafulvalene COFs for CO_2 conversion with H_2O without the addition of photosensitizers, sacrificial agents or noble metal cocatalysts. The photogenerated e^- were effectively transferred from tetrathiafulvalene to porphyrin, which led to the separation of e^--h^+ pairs for CO_2 reduction and H_2O oxidation. As a result, a photocatalytic CO production rate of 123.3 μmol·g^{-1} with a selectivity of 100% was achieved, along with H_2O oxidation to O_2 under the illumination of visible light after 60 h.

Fang *et al.*[114] reported a pyrazolyl porphyrinic Ni-MOF (PCN-601) that integrated a light photosensitizer, active sites and large surface areas as an excellent and durable photocatalyst for visible-light-driven CO_2 conversion with H_2O vapor. The production rate of CH_4 was much higher than that of similar MOFs based on carboxylate porphyrin.

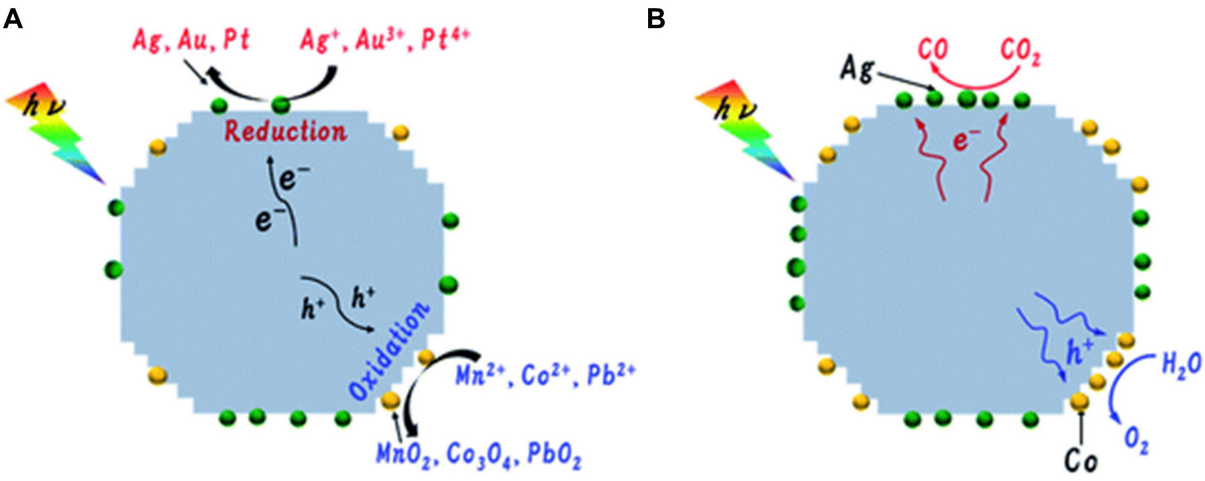

Figure 13. (A) Cocatalyst loading by the photodeposition method. (B) Photocatalytic CO_2 conversion into CO over Al-$SrTiO_3$ modified with Ag and Co using water as the reductant. Reproduced from Ref.[111] with permission from the Royal Society of Chemistry.

Heterometallic Fe_2M cluster-based MOF (NNU-31-M, M = Co, Ni and Zn) photocatalysts were fabricated by Dong *et al.*[115]. The overall conversion of CO_2 and H_2O into HCOOH and O_2 was achieved in the absence of any sacrificial agent and photosensitizer when using these MOFs. Under visible-light irradiation, the heterometallic clusters and photosensitive ligands can generate separated e^--h^+ pairs. The metal M accepts e^- to reduce CO_2 and the metal Fe uses h^+ to oxidize H_2O. NNU-31-Zn showed the highest HCOOH production of 26.3 $\mu mol \cdot g^{-1} \cdot h^{-1}$ and a selectivity of 100%.

Feng *et al.*[116] synthesized a Zr-based mixed-linker MOF (mPT-MOF), consisting of Zr clusters and 4,4'-(1,10-phenanthroline-3,8-diyl)dibenzoic acid and 2''-nitro-[1,1':4',1'':4'',1'''-quaterphenyl]-4,4'''-dicarboxylic acid linkers. Cu^I photosensitizers (Cu-PSs) and molecular Re catalysts were incorporated in the MOF to form mPT-Cu/Re for photocatalytic CO_2 reduction with water. Installation of the Cu-PSs and molecular Re catalysts in the MOF promoted the transfer of multi-electrons to drive CO_2 reduction under visible-light irradiation. A turnover number of 1328 was obtained, which was a 95-fold improvement over the homogeneous counterparts.

Jiang *et al.*[117] created "molecular compartments" inside MOF crystals by growing TiO_2 inside different pores of a chromium (Cr) terephthalate-based MOF (MIL-101) and its derivatives. This allows for the synergy between the light-absorbing/electron-generating TiO_2 units and the catalytic metal Cr clusters in the MOFs, thus facilitating the photoreduction of CO_2 to CO and CH_4 with the production of O_2 from H_2O. An AQE of 11.3% for CO_2 reduction at λ = 350 nm was obtained over 42%-TiO_2-in-MIL-101-Cr-NO_2 (42% of TiO_2 in a MIL-101 derivative).

Very recently, Yu *et al.*[118] integrated MoS_2 NSs into defective MOFs (d-UiO-66) to form Mo-O-Zr bimetallic sites between UiO-66 and MoS_2. The active interfaces were beneficial for the transfer of photogenerated charge carriers, resulting in enhanced activity. The d-UiO-66/MoS_2 composite facilitated visible-light-driven CO_2 conversion with H_2O to CH_3COOH. The production rate of CH_3COOH was 39.0 $\mu mol \cdot g^{-1} \cdot h^{-1}$ and the selectivity was 94%.

Wu *et al.*[119] reported Cu-based MOF, $Cu_3(BTC)_2$ (BTC = 1,3,5-benzene tricarboxylate), encapsulated Cu_2O nanowires for the photoreduction of CO_2 to CH_4 with water vapor. Such a MOF not only inhibits the water

vapor-induced corrosion of Cu_2O but also facilitates CO_2 uptake and charge separation [direct transfer of photogenerated electrons from the CB of Cu_2O to the LUMO level of non-excited $Cu_3(BTC)_2$], thus leading to a 1.9-fold higher photoactivity of CO_2 reduction into CH_4, compared to that of pure Cu_2O.

III. Nitride-based photocatalysts

Li *et al.*[120] incorporated the heteroatom B-Co dimer into a porous C_2N to form B-Co@C_2N, which was used for the photoreduction of CO_2 to C_2H_6. The combination of B and Co regulated the 3d orbital of the Co atoms to a lower energy level, which impairs the CO adsorption strength in comparison with Co-Co@C_2N and results in a low energy barrier of ~0.61 eV for C-C coupling. The H_2 production reaction was inhibited owing to the strong adsorption of the $*CO_2$/*COOH intermediates. Furthermore, the light absorbance of B-Co@C_2N in the visible and infrared light regions was improved in comparison with that on pure C_2N.

A Au/p-GaN photocatalyst with a plasmonic heterostructure realized the photoreduction of gas-phase CO_2 to CO with water oxidation under solar illumination[121]. This heterostructure photocatalyst was composed of metal/insulator/semiconductor components with an Al_2O_3 layer between the metal nanoparticles and p-GaN, which contributed to the promotion of CO production.

IV. Other photocatalysts

Wang *et al.*[122] fabricated a marigold-like SiC@MoS_2 photocatalyst with a unique Z-scheme structure to realize visible-light-driven CO_2 conversion with water. The production rates of CH_4 and O_2 were 323 and 621 $\mu L \cdot g^{-1} \cdot h^{-1}$, respectively, with stability over five cycles of 40 h.

Layered bismuth oxyhalides (BiOX, where X = F, CI, Br and I) were used for the conversion of CO_2 with H_2O without adding photosensitizers or sacrificial agents[123]. The optimal BiOBr photocatalyst displayed CO and CH_4 production rates of 21.6 and 1.2 $\mu mol \cdot g^{-1} \cdot h^{-1}$, respectively, under simulated sunlight irradiation.

SnS-SnS_2 heterostructured NS frameworks were grown on FTO substrates for the photoconversion of CO_2 with H_2O to C_2 (acetaldehyde) and C_3 (acetone) hydrocarbons[124]. The photoactivity of SnS-SnS_2 was improved by increasing the fraction of SnS in the composite through the partial transformation of SnS_2 to SnS. SnS provides CO_2 adsorption sites with lower activation energy, which is the rate-determining step for CO_2 reduction. The Z-scheme charge transfer dynamic in the SnS-SnS_2 catalyst drives the water oxidation on SnS_2 and CO_2 reduction on SnS.

Photocatalytic CO_2 conversion with H_2

Photocatalytic CO_2 conversion with H_2 is a prospective method for CO_2 reduction[125]. Light illumination can achieve a favorable rate and yield in eight-electron CO_2 reduction with H_2[125,126]. The photogenerated h^+ in the active VB of the photocatalysts can react with H_2 to produce H^+. The produced H^+ and photogenerated e^- can then convert CO_2 into CO, CH_3OH and hydrocarbons (e.g., CH_4, C_2H_4, C_2H_6, C_3H_6 and C_3H_8). Generally, CH_4 or CO products are produced during photocatalytic CO_2 conversion with H_2 (Equations 7 and 8)[89].

$$CO_2 + 4H_2 \rightarrow CH_4 + 2H_2O \quad (7)$$

$$CO_2 + H_2 \rightarrow CO + H_2O \quad (8)$$

In 2018, Jelle *et al.*[127] fabricated highly dispersed nanostructured RuO_2 catalysts loaded on 3D silicon photonic crystal supports for photocatalytic conversion of CO_2 with H_2 to CH_4. A conversion rate of 4.4 $mmol \cdot g_{cat}^{-1} \cdot h^{-1}$ was obtained under simulated solar irradiation. Silicon photonic crystals have unique light-harvesting characteristics in the entire spectrum of sunlight, coupled with its large surface area, resulting in the high CH_4 production rate. In the same year, Wang *et al.*[128] reported a defect-rich indium oxide [$In_2O_{3-x}(OH)_y$] catalyst for the light-driven reduction of CO_2 to CH_3OH. The CH_3OH production rate and selectivity were 0.06 $mmol \cdot g_{cat}^{-1} \cdot h^{-1}$ and 50%, respectively, under simulated solar irradiation. Furthermore, in 2019, Yan *et al.*[129] used the rhombohedral polymorph of an indium sesquioxide photocatalyst for the photocatalytic reduction of CO_2 to CH_3OH and CO. Notably, the rhombohedral polymorph exhibited higher photoactivity, superior stability and improved selectivity toward CH_3OH over CO. In 2020, Yan *et al.*[130] reported the isomorphic replacement of Lewis acid sites (In^{3+} ions) in In_2O_3 with single-site Bi^{3+} ions to activate CO_2 molecules. The as-formed $Bi_xIn_{2-x}O_3$ photocatalyst showed a three orders of magnitude higher photoactivity than In_2O_3 itself and also exhibited significant photoactivity for CH_3OH production. The enhanced photoactivity was attributed to the increased solar energy utilization rate and rapid separation and transfer of photogenerated charges.

Photocatalytic CO_2 conversion with methane reforming

Methane (CH_4) is the second most common greenhouse gas[89]. The photocatalytic conversion of CO_2 into syngas (H_2 and CO) with CH_4 reforming (Equation 9) is considered an effective method to decrease the environmental concentration of these two greenhouse gases. Generally, metal catalysts are highly effective for this reaction.

$$CO_2 + CH_4 \rightarrow 2H_2 + 2CO \quad (9)$$

Huang *et al.*[131] reported the conversion of CO_2 by CH_4 upon a Ni nanocrystal modified with silica clusters, which exhibited excellent durability for methane reforming (> 700 h). It achieved high H_2 and CO production rates of 17.1 and 19.9 $mmol \cdot g^{-1} \cdot min^{-1}$, respectively, and excellent solar fuel efficiency of 12.5% under solar light irradiation. Even under IR irradiation (λ > 830 nm), the solar-to-fuel efficiency remained at 3.1%.

Zhou *et al.*[132] loaded single-atom Ru sites on a Cu nanoparticle surface for photocatalytic CO_2 conversion with CH_4 reforming. A stability of 50 h and a selectivity of > 99% were achieved. Photoexcited hot carriers and single-atom Ru active sites led to the observed photoactivity.

Shoji *et al.*[133] reported a $SrTiO_3$-supported Rh catalyst for UV-light-driven CO_2 reduction with CH_4 reforming, which cannot be realized by traditional thermal catalysis. The photogenerated h^+ and e^- were employed for the oxidation of CH_4 over $SrTiO_3$ and the reduction of CO_2 over Rh, respectively.

The photoassisted steam reforming and dry CO_2 reforming of CH_4 at room temperature with high selectivity of syngas were realized in gas-phase catalysis by Zhao *et al.*[134] for the first time. Bimetallic Rh-V oxide cluster anions ($Rh_2VO_{1-3}^-$) were used as catalysts and both the oxidation of CH_4 and the reduction of H_2O/CO_2 were achieved effectively without light irradiation. The key step in controlling the syngas (CO and H_2) selectivity in this system was to photoinduce the reaction intermediates ($Rh_2VO_{2,3}CH_2^-$) into electronically excited states [Figure 14][134].

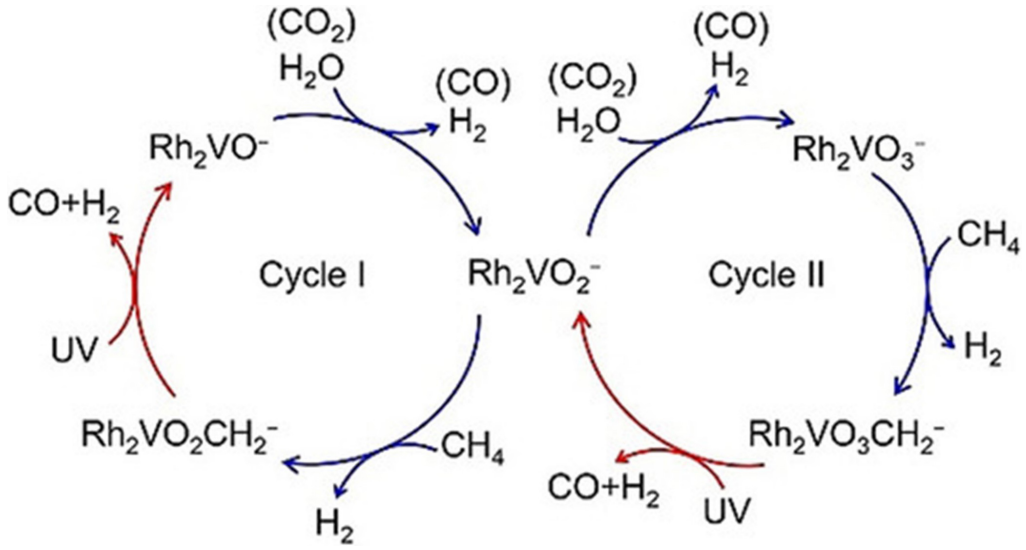

Figure 14. Two consecutive catalytic cycles of photoassisted steam reforming or dry CO_2 reforming of methane to syngas mediated by $Rh_2VO_{1-3}^-$ clusters. "UV" represents ultraviolet light (λ = 355 nm photon). Reproduced from Ref.[134] with permission from Wiley.

Photocatalytic CO_2 conversion with other electron donors

TEOA, TEA, triisopropanolamine (TIPA) and sodium sulfite (Na_2SO_3) have been reported as efficient electron donors for quenching the photogenerated h^+ during photocatalytic CO_2 conversion.

I. TEOA as an electron donor

The growth and assembly of highly dispersed UiO-66-NH_2 nanocrystals upon graphene to form an active photocatalyst for CO_2 conversion was reported by Wang *et al.*[135]. The as-synthesized UiO-66-NH_2 /graphene photocatalyst displayed both high activity and selectivity for the visible-light-driven conversion of CO_2 to HCOOH in the presence of TEOA. The photoreduction efficiency of UiO-66-NH_2/graphene for CO_2 was ~11 times greater than that of UiO-66-NH_2. The strong interaction between UiO-66-NH_2 and graphene effectively boosted the transfer of photogenerated e^- and inhibited the separation of UiO-66-NH_2 from graphene, resulting in its high photoactivity and good cyclability.

Wang *et al.*[136] confined highly dispersed nickel cobalt oxyphosphide nanoparticles (NiCoOP NPs) in multichannel hollow carbon fibers (MHCFs) to form a NiCoOP-NP@MHCF catalyst for photocatalytic CO_2 reduction. The photoactivity was investigated in a tandem system, with $[Ru(bpy)_3]Cl_2{\cdot}6H_2O$ (bpy = 2′2-bipyridine) used as a photosensitizer in the presence of TEOA. The as-formed catalyst exhibited considerable activity, offering a CO production rate of 166 $\mu mol{\cdot}mg_{cat}^{-1}{\cdot}h^{-1}$.

Wang *et al.*[137] decorated single-atom Cu sites upon UiO-66-NH_2 (Cu SAs/UiO-66-NH_2) to promote the photoreduction of CO_2 to liquid fuels, with TEOA used as an electron donor. The decoration of single-atom Cu sites on UiO-66-NH_2 facilitated the conversion of CO_2 to CHO* and CO* intermediates, resulting in good selectivity for CH_3OH and CH_3CHOH. This photocatalyst realized CH_3OH and CH_3CH_2OH production rates of 5.33 and 4.22 $\mu mol{\cdot}g^{-1}{\cdot}h^{-1}$, respectively, which were much higher compared to those of pure UiO-66-NH_2 and Cu NP-loaded UiO-66-NH_2.

Yang *et al.*[138] demonstrated that a Ni-based metal-organic layer (MOL) exposing rich (100) crystal facets (Ni-MOL-100) showed much higher CO_2-to-CO photoactivity than with rich (010) crystal facets exposed

(Ni-MOL-010) and bulky Ni-MOF. Under Xe lamp irradiation (300 mW, $\lambda > 420$ nm), the catalytic activity in a $[Ru(phen)_3](PF_6)_2$, TEOA, CH_3CN and H_2O system reached 2.5- and 4.6-fold higher than those of Ni-MOL-010 and bulky Ni-MOF, respectively.

Li *et al.*[139] presented a bioinspired MOF with flexible Cu and Ni dual-metal-site pairs (DMSPs) that exhibited self-adaptive behavior to fit mutative C1 intermediates, realizing visible-light-driven CO_2 reduction to CH_4. The Cu and Ni DMSPs were incorporated into MOF-808 to form MOF-808-CuNi, leading to a production rate of 158.7 $\mu mol \cdot g^{-1} \cdot h^{-1}$ and a promoted CH_4 selectivity of 97.5%. Various C1 intermediates were stabilized by the flexible self-adaptive DMSPs in multistep reactions, resulting in the high selectivity of CH_4.

II. TEA as an electron donor

Qi *et al.*[140] proposed a single molecular cage of Ir(III) complex-decorated Zr-based metal-organic cages (Ir^{III}-MOC-NH_2) for visible-light-driven CO_2 reduction. The Ir^{III}-MOC-NH_2 catalyst had high photoactivity and selectivity for CO_2-to-CO conversion in the presence of TEA. The selectivity was 99.5% and the turnover frequency reached ~120 h^{-1}, which was 3.4 times that of bulk Ir^{III}-MOC-NH_2. The AQE was 6.71%.

III. TIPA as an electron donor

Liu *et al.*[141] reported three functionalized polyoxo-titanium cluster-based photocatalysts for CO_2 reduction, namely, Ti_6 functionalized with phenylphosphonic acid and Ti_8 and Ti_6 functionalized with 1,1-ferrocene dicarboxylic acid (Fcdc). The light absorption range of Ti_8-Fcdc and Ti_6-Fcdc was expanded to the visible light region. The introduction of Fcdc ligands in the photocatalysts boosted the transfer of electrons from the Fcdc ligands to the Ti-oxo nucleus. In particular, both Ti_8-Fcdc and Ti_6-Fcdc achieved the photocatalytic reduction of CO_2 to $HCOO^-$ with high selectivity (96.2% and 97.5%, respectively) and photoactivity (170.30 and 350.00 $\mu mol \cdot g^{-1} \cdot h^{-1}$, respectively) under visible-light irradiation in the presence of TIPA.

IV. Sodium sulfite (Na_2SO_3) as an electron donor

Zhu *et al.*[142] prepared a Cu/Cu^+-modified Ti^{3+}/TiO_2 (Cu/Cu^+@TiO_2) photocatalyst for photocatalytic CO_2 conversion under Xe lamp irradiation with Na_2SO_3 as an electron donor. The Cu^+-O valences inside the TiO_2 lattice promoted the transfer of carriers and the Cu on the surface of the catalyst as active sites promoted the reduction of CO_2. The synergistic effect between Cu and Cu^+ ions increased the charge carrier density. All the photogenerated e^- in the photocatalyst (100%) were used for CO_2 reduction.

Photocatalytic H_2O_2 production

Basic principles of photocatalytic H_2O_2 production

Since H_2O_2 was first synthesized in 1818[143], it has captured more and more attention and has even been listed as one of the 100 most important chemicals[144]. As a green oxidant, H_2O_2 contains a 47.1% (w/w) active oxygen content. Apart from H_2O and O_2, no other byproducts are generated during its reactions. As a result, H_2O_2 has been widely used in organic synthesis[145], wastewater treatment and disinfection[146] and the pulp and paper industry[147]. Moreover, H_2O_2 has also been employed in energy research as a one-compartment fuel cell[148]. The theoretical maximum output potential of 1.09 V in H_2O_2 fuel cells is comparable to that in conventional H_2 fuel cells (1.23 V). However, unlike H_2, H_2O_2 is completely soluble in water and easy to transport, which paves the way for it to become a desirable alternative energy carrier. These wide applications result in a huge demand for H_2O_2, with the global annual demand at ~2.2 Mt[149].

At present, anthraquinone oxidation is the primary technology for industrial H_2O_2 production[143]. However, its industrial synthetic route is complicated, with high energy consumption and toxic byproducts.

Alternative approaches are in development, such as the direct production of H_2O_2 from O_2 and H_2, but this method has a high cost, high energy intensity and a risk of explosions. Compared with these two methods, photocatalytic H_2O_2 production requires only earth-abundant H_2O or other sacrificial agents and O_2 as raw materials instead of dangerous H_2/O_2 mixtures and can be operated using semiconductors as catalysts under sunlight irradiation[150-153]. Moreover, no pollutants are produced during this process.

A detailed illustration of photocatalytic H_2O_2 production is presented in Figure 15[9]. The photogenerated h^+ in the VB oxidizes H_2O (or other sacrificial agents) to generate O_2 (or other oxidation products) and protons (H^+, Equation 10), while the photogenerated e^- in the CB reacts with the adsorbed O_2 to generate H_2O_2. Specifically, H_2O_2 can be produced through either an indirect sequential two-step one-electron reduction route (Equations 11 and 12) or a direct one-step two-electron reduction route (Equation 13). In the indirect two-step one-electron reduction process, the one-electron reduction of O_2 produces a superoxide radical ($O_2^{\bullet-}$, Equation 11), which then reacts with two H^+ ions and another electron to produce H_2O_2 (Equation 12). In the direct one-step two-electron reduction of O_2 to H_2O_2, O_2 reacts directly with two H^+ ions to form H_2O_2 via a two-electron reduction process (Equation 13). These two processes can both be described by the overall reaction in Equation 14.

$$2H_2O + 4h^+ \rightarrow O_2 + 4H^+ (10)$$

$$O_2 + e^- \rightarrow O_2^{\bullet-} (11)$$

$$O_2^{\bullet-} + 2H^+ \rightarrow H_2O_2 (12)$$

$$O_2 + 2H^+ + 2e^- \rightarrow H_2O_2 (13)$$

$$2H_2O + O_2 \rightarrow 2H_2O_2 (14)$$

Recent advances in photocatalytic H_2O_2 production

H_2O_2 production from O_2 reduction

I. C_3N_4-based photocatalysts

An interfacial Schottky junction consisting of Ti_3C_2 and porous g-C_3N_4 NSs was designed by Yang *et al.*[154] for visible-light-driven H_2O_2 production. It displayed an H_2O_2 production rate of 2.20 μmol·L^{-1}·min^{-1}, which was ~2.1 times that of pure g-C_3N_4. The improved photoactivity was ascribed to the formed interfacial Schottky junction and built-in electric field, which boosted the spatial separation of photogenerated charges.

Wu *et al.*[155] introduced alkali metal dopants and N vacancies in C_3N_4. This extended the light absorption region, shortened the band gap from 2.85 to 2.63 eV and suppressed the recombination of photogenerated charges. The synergistic effect of the dopants and defects brought about a photocatalytic H_2O_2 production rate of 10.2 mmol·g^{-1}·h^{-1} using isopropanol as an electron donor, which was 89.5 times that of pure C_3N_4. Similarly, Xie *et al.*[156] introduced two types of cooperative N vacancies, that is, NH_x and N_2C vacancies, into polymeric carbon nitride. It delivered a 15-fold improvement in H_2O_2 production with excellent stability using ethanol as a sacrificial hole scavenger. The AQE reached 26.78% and 11.86% at 340 and 420 nm, respectively. The NH_x and N_2C vacancies accelerated the photoexcited charge separation and assisted in activating O_2 in the two-electron pathway, respectively.

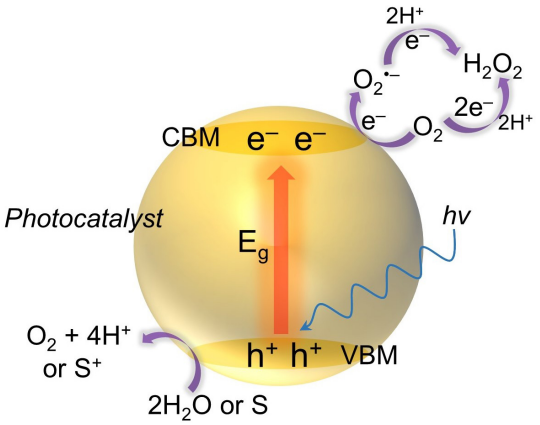

Figure 15. Illustration of photocatalytic H_2O_2 production. S represents the sacrificial agents. CBM: Conduction band minimum; VBM: valence band maximum.

Zhang *et al.*[157] prepared an alkali and sulfur codoped polymeric carbon nitride and used it as a photocatalyst for H_2O_2 production from the O_2 reduction reaction. The photocatalyst realized a H_2O_2 production rate on the millimolar level under the irradiation of visible light with an AQE of 100% and a selectivity of 96%. Alkali and sulfur dopants in the photocatalyst boosted the separation of interlayer charges and the polarization of trapped electrons for the capture and reduction of O_2, respectively.

Zhou *et al.*[158] synthesized surface •OH group-functionalized g-C_3N_4 nanotubes. The nanotube structures provided a high surface area and promoted mass transfer. The •OH groups captured the photogenerated h^+ to facilitate the separation of photogenerated charges and were also beneficial in suppressing the self-decomposition of H_2O_2. Consequently, a H_2O_2 production rate of 240.36 $\mu mol \cdot g^{-1} \cdot h^{-1}$ was obtained.

Chen *et al.*[159] prepared a Na^+-doped cyano-rich g-C_3N_4 photocatalyst. The porous g-C_3N_4 with Na^+ dopants and cyano groups simultaneously optimized the photoactivity and selectivity, showing H_2O_2 production rates of 7.01 $mmol \cdot h^{-1}$ under visible light irradiation ($\lambda \geq 420$ nm) and 16.05 $mmol \cdot h^{-1}$ under simulated sun conditions, respectively, and a selectivity of 93% from two-electron O_2 reduction.

II. MOF- and COF-based photocatalysts

In 2018, Isaka *et al.*[160] reported the visible-light-driven H_2O_2 production via two-electron O_2 reduction using a MIL-125-NH_2 photocatalyst with TEOA or benzyl alcohols as electron donors. Depositing NiO nanoparticles upon MIL-125-NH_2 drastically improved its photoactivity. Furthermore, in 2021, Chen *et al.*[161] introduced a photosensitizer, 4,4,4′,4″-(pyrene-1,3,6,8-tetrayl)tetrabenzoic acid (L2), into MIL-125 to form L2-functionalized MOFs (MIL-125-L2), which showed a H_2O_2 production rate of 1654 $\mu mol \cdot L^{-1} \cdot h^{-1}$ under the illumination of visible light ($\lambda > 400$ nm) with TEOA as a sacrificial hole scavenger. This high photoactivity was ascribed to the visible light absorption of L2, which originated from the π-electron system in L2, making MIL-125-L2 a catalyst for visible light response.

In 2020, Krishnaraj *et al.*[162] reported two new 2D COFs, in which the (diarylamino)benzene linkers formed a Kagome lattice and showed strong visible light absorption. The high crystallinity and large surface area of these COFs allowed for effective charge transfer and diffusion. The diarylamine (donor) unit in these COFs efficiently promoted the reduction of O_2 to H_2O_2 using alcohols as sacrificial hole scavengers.

H_2O_2 production from O_2 reduction coupled with value-added organic chemical synthesis from organic matter oxidation

The production of H_2O_2 from O_2 reduction coupled with the synthesis of value-added organic chemicals is attractive. On this basis, photogenerated carriers can be fully utilized during the process of photocatalytic renewable energy production, enhancing the processes of solar-to-chemical conversion efficiency.

I. Reduction of O_2 coupled with oxidation of benzyl alcohol

Benzaldehyde is the simplest and most important aromatic aldehyde in industry. It has a wide range of applications in medicine, dyes, perfumes, resins and other industries[163]. The photocatalytic production of benzaldehyde from the oxidation of benzyl alcohol is a green process (Equation 15).

$$O_2 + Ph\text{-}CH_2OH \rightarrow H_2O_2 + Ph\text{-}CHO \quad (15)$$

In 2019, Isaka *et al.*[164] reported hydrophobic linker-alkylated MOFs, MIL-125-Rn (n = 4 and 7), for the photocatalytic production of H_2O_2 in a two-phase system (water/benzyl alcohol) [Figure 16A and B]. The hydrophobization of MIL-125-NH_2 separated it from the aqueous phase into the benzyl alcohol phase. In this two-phase system, H_2O_2 was produced in the water phase, while the MOF structure was more stable in the benzyl alcohol phase. This resulted in improved photoactivity [Figure 16C]. The as-prepared hydrophobic MOF also showed its feasible application in H_2O_2 production in various aqueous solutions, including extremely low pH and NaCl solutions [Figure 16D]. Furthermore, Kawase *et al.*[165] reported another hydrophobic cluster-alkylated MIL-125-NH_2 (OPA/MIL-125-NH_2). Its Ti clusters were alkylated by octadecylphosphonic acid (OPA). The activity for H_2O_2 production was higher than that of the reported MIL-125-Rn in the abovementioned two-phase system[164]. OPA modified the outermost surface of the MOFs while preserving the inner pores, which resulted in enhanced activity. In 2020, Chen *et al.*[166] further synthesized a hydrophobic OPA/$Zr_{100-x}Ti_x$-MOF (x = 0, 5, 7.5 and 10), in which Zr clusters were alkylated with OPA, and applied it for H_2O_2 production in the above-mentioned two-phase system. The optimal OPA/$Zr_{92.5}Ti_{7.5}$-MOF photocatalyst displayed a H_2O_2 production rate of 9.7 mmol·L^{-1}·h^{-1} under the illumination of visible light (λ > 420 nm), which was ~4.5 times that of the Zr_{100}-MOF. H_2O_2 production cycling tests indicated that it showed good stability.

II. Reduction of O_2 coupled with oxidation of benzylamine

The synthesis of nitriles from the selective oxidation of amines plays a key role in both laboratory and industrial synthetic processes because nitrile is an important intermediate product for the synthesis of several fine chemicals, pharmaceuticals and agrochemicals[167-173]. The photocatalytic oxidation of amines to nitriles is an effective approach for the synthesis of nitriles under mild conditions (Equation 16).

$$2O_2 + Ph\text{-}CH_2NH_2 \rightarrow 2H_2O_2 + Ph\text{-}CN \quad (16)$$

In 2021, Tian *et al.*[174] reported that benzylamine oxidation could be used as a half-reaction to couple with H_2O_2 production from O_2 reduction (Equation 13) using defective ZrS_3 nanobelts with disulfide (S_2^{2-}) and sulfide anion (S^{2-}) vacancies [Figure 17A-F]. The defective ZrS_3 nanobelts exhibited good photoactivity for H_2O_2 production and high selectivity (> 99%) for benzonitrile production from benzylamine oxidation [Figure 17G and H]. The S_2^{2-} vacancies facilitated the separation of e^--h^+ pairs and the S^{2-} vacancies improved the e^- conduction, h^+ extraction and benzylamine oxidation kinetics. As a result, the photocatalyst displayed a H_2O_2 production rate of 78.1 ± 1.5 and a benzonitrile production rate 32.0 ± 1.2 μmol·h^{-1} under simulated sunlight irradiation.

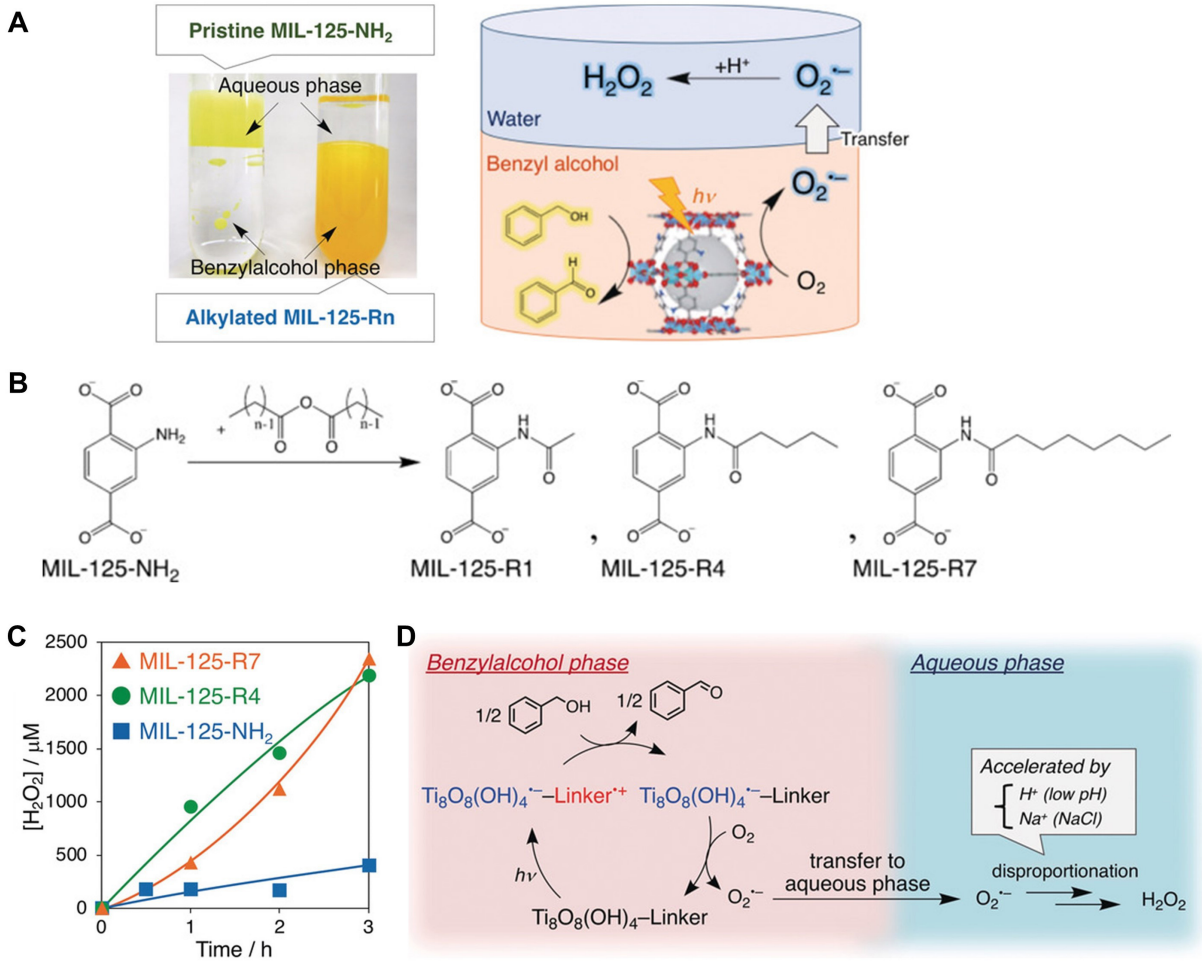

Figure 16. (A) Two-phase system (water/benzyl alcohol) for photocatalytic H_2O_2 production. (B) Alkylation reaction of linkers of MIL-125-NH_2 to form MIL-125-R*n* (*n* = 1, 4 or 7). (C) Photocatalytic activity and (D) related mechanism of H_2O_2 production in the two-phase system under photoirradiation (λ > 420 nm). Reproduced from Ref.[164] with permission from Wiley.

H_2O_2 production from O_2 and H_2O

To improve the eco-friendliness and sustainability of H_2O_2 production, earth-abundant water should be used instead of alcohols or other sacrificial agents (e.g., TEOA and TEA). The oxidation of H_2O by h^+ produces O_2 and H^+, while the reduction of O_2 by e^- produces H_2O_2[175]. On this basis, H_2O_2 can be synthesized from H_2O and O_2 with 100% efficiency.

Ma *et al.*[176] fabricated a protonated TiO_2 nanotube with carbon dots for H_2O_2 production under visible-light irradiation (λ > 420 nm). It showed a H_2O_2 production rate of 3.42 mmol·g_{cat}^{-1}·h^{-1} in water, exceeding the values obtained on TiO_2 catalysts with noble metals. The protons on the catalyst play a key role in H_2O_2 production by promoting the reduction of O_2 to H_2O_2 and inhibiting H_2O_2 decomposition. This catalyst displayed a solar-to-H_2O_2 apparent energy conversion efficiency of 5.2%.

Zeng *et al.*[177] reported a C_3N_4-grafted cationic polyethylenimine (PEI) molecule for the photocatalytic H_2O_2 production from H_2O and O_2. The PEI/C_3N_4 photocatalyst exhibited a H_2O_2 production rate of 208.1 μmol·g^{-1}·h^{-1}, which was 25 times that of the pure C_3N_4. This was ascribed to the simultaneous improvement in charge separation and two-electron O_2 reduction selectivity.

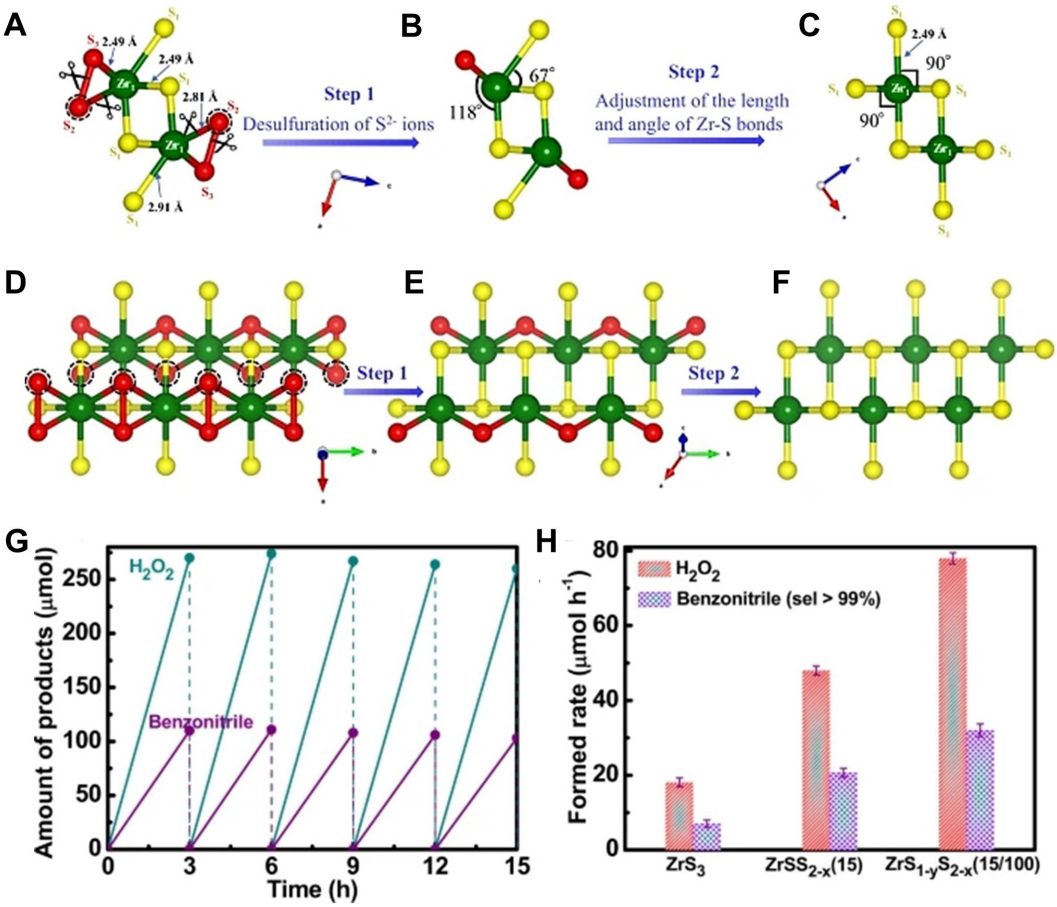

Figure 17. Transformation process of monoclinic ZrS_3 into hexagonal ZrS_2 from the [010] (A-C) and [001] (D-F) views. (A, D) Crystal structure of monolayer ZrS_3 with a boundary of 1 × 3 × 1. (B, E) Crystal structure of monolayer ZrS_3 after desulfuration of S_2^{2-} ions. (C, F) Crystal structure of monolayer ZrS_2 with a boundary of 1 × 3 × 1. (G) Activity of H_2O_2 and benzonitrile production for a repeated photoreaction sequence with $ZrS_{1-y}S_{2-x}$ (15/100) under simulated sunlight irradiation [$ZrSS_{2-x}$ annealed for X time was denoted as $ZrSS_{2-x}$(X), and $ZrS_{1-y}S_{2-x}$ annealed for X min and treated with Y mg Li was denoted as $ZrS_{1-y}S_{2-x}$(X/Y)]. (H) H_2O_2 and benzonitrile production rates. Reproduced from Ref.[174] with permission from Springer Nature.

In 2020, Zhao *et al.*[178] demonstrated a ZIF-8/C_3N_4 composite for visible-light-driven H_2O_2 production from H_2O and O_2. It displayed a H_2O_2 production rate of 2641 μmol·g^{-1}·h^{-1} and an AQE of 19.57%. In 2021, Zhao *et al.*[179] constructed a C_3N_4-assisted $Ni_3(HHTP)_2$ (Ni-CAT) photocatalyst that could catalyze the production of H_2O_2 from H_2O and O_2 under visible-light illumination. In this case, the Ni-CAT photocatalyst was the main active component for the reduction of O_2, while C_3N_4-assisted Ni-CAT suppressed the recombination of photogeneration charge carriers by providing electrons. Furthermore, Wu *et al.*[180] fabricated a metal-free photocatalyst composed of carbon dots, organic dye molecules, procyanidins and 4-methoxybenzaldehyde for direct H_2O_2 production from seawater. This catalyst exhibited a visible-light-driven H_2O_2 production rate of 1776 μmol·g^{-1}·h^{-1}, which is ~4.8 times that of the pristine polymer.

In 2021, Teng *et al.*[181] fabricated a Sb-single-atom-loaded C_3N_4 photocatalyst for the production of H_2O_2 from water and O_2 at λ = 420 nm. An AQE of 17.6% and a conversion efficiency of solar energy to chemical energy of 0.61% for H_2O_2 production were achieved. The formed μ-peroxide at the Sb sites promoted the two-electron O_2 reduction reaction and highly concentrated photogenerated h^+ at its neighboring N atoms promoted water oxidation reaction, resulting in the excellent photocatalytic activity. Importantly, in the

same year, Ye *et al.*[182] reported a zinc polyphthalocyanine (ZnPPc)-decorated and B-doped carbon nitride (NBCN) hybrid (ZnPPc-NBCN) photocatalyst with a Z-scheme heterostructure. The high redox potential of the photocatalyst was stable during the reaction and the photocatalytic H_2O_2 production rate from pure water and open air reached 114 $\mu mol \cdot g^{-1} \cdot h^{-1}$.

CONCLUSIONS AND OUTLOOK

This review summarizes recent significant achievements in photocatalytic renewable energy production based on semiconductor and semiconductor-like driven photocatalysis, particularly for H_2 production, CO_2 reduction and H_2O_2 generation. To improve the photocatalytic performance, these research works have mainly focused on solving two scientific issues with photocatalysis, namely, light absorption and photogenerated charge separation. To improve the light utilization rate and/or boost the photogenerated charge separation, various strategies based on the design of photocatalysts have been employed: (1) doping of heteroelements/modification with single atoms; (2) creation of defects; (3) loading of dual cocatalysts; (4) construction of heterostructures (e.g., type II and Z-scheme); (5) fabrication of isotropic facets; and (6) generation of synergistic effects using multicomponents. Meanwhile, the improvement on the following reactions has also been considered: (1) for H_2 production from overall water splitting: effective water oxidation half-reaction and separation of the H_2 and O_2 products; (2) for CO_2 conversion: solubility and competitive H_2 production in the liquid phase, activation of CO_2 molecules and product selectivity; and (3) for H_2O_2 production from O_2 (and water): the selectivity of two-electron O_2 reduction, effective water oxidation half-reaction and self-decomposition of the formed H_2O_2.

The current semiconductor-based nanocomposite systems mainly consist of single inorganic semiconductor components or organic semiconductor-like polymers, such as MOFs and COFs. Although significant advances in photocatalytic renewable energy production have been achieved, these systems still exhibit some shortcomings, including the photocorrosion of sulfides and the instability of MOF and COF structures. For practical applications, it is necessary to bestow these traditional systems with new features or functionality in future research.

(1) Semiconductor-based bioinspired photocatalysis is a promising avenue for new photocatalysts with enhanced efficiency and stability, inspired by the abovementioned bioinspired HER-WOR-MOF photocatalyst[79]. Such a system can be constructed by the effective integration of the superiorities from traditional photocatalysis and biological components, that is, the combination of traditional inorganic semiconductors and highly selective bioenzymes.

(2) Photoelectrocatalysis that can efficiently combine photo- and electric energies represents an important direction, inspired by the aforementioned hydrogen farm project[83]. Such strategies can efficiently enhance the catalytic efficiency and easily separate the catalysts and products.

(3) Photothermal catalysis is another exciting direction. For example, the conversion of CO_2 with H_2 or CH_4 via thermal catalysis requires high temperatures. Introducing photocatalysis can lower the temperature. Thus, the combination of photocatalysis and thermal catalysis is of great significance for future research.

DECLARATIONS

Authors' contributions

Wrote the manuscript: Chen X, Zhao J

Reviewed the manuscript: Zhang D, Li G, Li H

Availability of data and materials
Not applicable.

Financial support and sponsorship
This work was supported by the National Key Research and Development Program of China (2020YFA0211004), and National Natural Science Foundation of China (22022608, 21876112, 21876113, 92034301), "111" Innovation and Talent Recruitment Base on Photochemical and Energy Materials (No. D18020), Ministry of Education, and Shanghai Key Laboratory of Rare Earth Functional Materials, Shanghai Engineering Research Center of Green Energy Chemical Engineering (No. 18DZ2254200), Shanghai Frontiers Science Research Base of Biomimetic Catalysis and Shanghai government (18SG41).

Conflicts of interest
All authors declared that there are no conflicts of interest.

Ethical approval and consent to participate
Not applicable.

Consent for publication
Not applicable.

REFERENCES
1. Martins F, Felgueiras C, Smitkova M, Caetano N. Analysis of fossil fuel energy consumption and environmental impacts in European countries. *Energies* 2019;12:964. DOI
2. Hisatomi T, Kubota J, Domen K. Recent advances in semiconductors for photocatalytic and photoelectrochemical water splitting. *Chem Soc Rev* 2014;43:7520-35. DOI PubMed
3. Wen M, Mori K, Kuwahara Y, An T, Yamashita H. Design and architecture of metal organic frameworks for visible light enhanced hydrogen production. *Appl Catal B-Environ* 2017;218:555-69. DOI
4. Cheng H, Wen M, Ma X, et al. Hydrogen doped metal oxide semiconductors with exceptional and tunable localized surface plasmon resonances. *J Am Chem Soc* 2016;138:9316-24. DOI PubMed
5. Bhatkhande DS, Pangarkar VG, Beenackers AA. Photocatalytic degradation for environmental applications - a review. *J Chem Technol Biotechnol* 2002;77:102-16. DOI
6. Fuku K, Hayashi R, Takakura S, Kamegawa T, Mori K, Yamashita H. The synthesis of size- and color-controlled silver nanoparticles by using microwave heating and their enhanced catalytic activity by localized surface plasmon resonance. *Angew Chem Int Ed Engl* 2013;52:7446-50. DOI PubMed
7. Cheng H, Qian X, Kuwahara Y, Mori K, Yamashita H. A plasmonic molybdenum oxide hybrid with reversible tunability for visible-light-enhanced catalytic reactions. *Adv Mater* 2015;27:4616-21. DOI PubMed
8. Kamegawa T, Shimizu Y, Yamashita H. Superhydrophobic surfaces with photocatalytic self-cleaning properties by nanocomposite coating of TiO(2) and polytetrafluoroethylene. *Adv Mater* 2012;24:3697-700. DOI PubMed
9. Hou H, Zeng X, Zhang X. Production of hydrogen peroxide by photocatalytic processes. *Angew Chem Int Ed Engl* 2020;59:17356-76. DOI PubMed
10. Low J, Yu J, Jaroniec M, Wageh S, Al-Ghamdi AA. Heterojunction photocatalysts. *Adv Mater* 2017;29:1601694. DOI PubMed
11. Wang F, Li Q, Xu D. Recent progress in semiconductor-based nanocomposite photocatalysts for solar-to-chemical energy conversion. *Adv Energy Mater* 2017;7:1700529. DOI
12. Zhao W, Chen Z, Yang X, et al. Recent advances in photocatalytic hydrogen evolution with high-performance catalysts without precious metals. *Renew Sustain Energy Rev* 2020;132:110040. DOI
13. Wang Z, Li C, Domen K. Recent developments in heterogeneous photocatalysts for solar-driven overall water splitting. *Chem Soc Rev* 2019;48:2109-25. DOI PubMed
14. Ou M, Li J, Chen Y, et al. Formation of noble-metal-free 2D/2D $Zn_mIn_2S_{m+3}$ (m = 1, 2, 3)/MXene Schottky heterojunction as an efficient photocatalyst for hydrogen evolution. *Chem Eng J* 2021;424:130170. DOI
15. Ou M, Li J, Geng M, Wang J, Wan S, Zhong Q. Construction of Z-scheme photocatalyst containing $ZnIn_2S_4$, Co_3O_4-photodeposited

$BiVO_4$ (110) facets and rGO electron mediator for overall water splitting into H_2 and O_2. *Catal Lett* 2021;151:2570-82. DOI
16. Wang L, Zhang J, Zhang Y, Yu H, Qu Y, Yu J. Inorganic metal-oxide photocatalyst for H_2O_2 production. *Small* 2021. DOI
17. Hejazi S, Mohajernia S, Osuagwu B, et al. On the controlled loading of single platinum atoms as a Co-catalyst on TiO_2 anatase for optimized photocatalytic H_2 generation. *Adv Mater* 2020;32:e1908505. DOI PubMed
18. Cho Y, Park B, Padhi DK, et al. Disordered-layer-mediated reverse metal-oxide interactions for enhanced photocatalytic water splitting. *Nano Lett* 2021;21:5247-53. DOI PubMed
19. Méndez-Medrano MG, Kowalska E, Ohtani B, et al. Heterojunction of CuO nanoclusters with TiO_2 for photo-oxidation of organic compounds and for hydrogen production. *J Chem Phys* 2020;153:034705. DOI PubMed
20. Osuagwu B, Raza W, Tesler AB, Schmuki P. A drastic improvement in photocatalytic H_2 production by TiO_2 nanosheets grown directly on Ta_2O_5 substrates. *Nanoscale* 2021;13:12750-6. DOI PubMed
21. Sun L, Zhuang Y, Yuan Y, et al. Nitrogen-Doped carbon-coated CuO-In_2O_3 p-n heterojunction for remarkable photocatalytic hydrogen evolution. *Adv Energy Mater* 2019;9:1902839. DOI
22. Han L, Jing F, zhang J, et al. Environment friendly and remarkably efficient photocatalytic hydrogen evolution based on metal organic framework derived hexagonal/cubic In2O3 phase-junction. *Appl Catal B-Environ* 2021;282:119602. DOI
23. Guo L, Yang Z, Marcus K, et al. MoS_2/TiO_2 heterostructures as nonmetal plasmonic photocatalysts for highly efficient hydrogen evolution. *Energy Environ Sci* 2018;11:106-14. DOI
24. Wang W, Zhu S, Cao Y, et al. Edge-enriched ultrathin MoS_2 embedded yolk-shell TiO_2 with boosted charge transfer for superior photocatalytic H_2 evolution. *Adv Funct Mater* 2019;29:1901958. DOI
25. Lai G, Lyu L, Huang Y, et al. Few-layer WS_2-MoS_2 in-plane heterostructures for efficient photocatalytic hydrogen evolution. *Nano Energy* 2021;81:105608. DOI
26. Xiao S, Dai W, Liu X, et al. Microwave-induced metal dissolution synthesis of core-shell copper nanowires/ZnS for visible light photocatalytic H_2 evolution. *Adv Energy Mater* 2019;9:1900775. DOI
27. Wang S, Zhu B, Liu M, Zhang L, Yu J, Zhou M. Direct Z-scheme ZnO/CdS hierarchical photocatalyst for enhanced photocatalytic H2-production activity. *Appl Catal B-Environ* 2019;243:19-26. DOI
28. Dai B, Fang J, Yu Y, et al. Construction of infrared-light-responsive photoinduced carriers driver for enhanced photocatalytic hydrogen evolution. *Adv Mater* 2020;32:e1906361. DOI PubMed
29. Zhang P, Luan D, Lou XWD. Fabrication of CdS frame-in-cage particles for efficient photocatalytic hydrogen generation under visible-light irradiation. *Adv Mater* 2020;32:e2004561. DOI PubMed
30. Ong WJ, Tan LL, Ng YH, Yong ST, Chai SP. Graphitic carbon nitride (g-C3N4)-based photocatalysts for artificial photosynthesis and environmental remediation: are we a step closer to achieving sustainability? *Chem Rev* 2016;116:7159-329. DOI PubMed
31. Ismael M. A review on graphitic carbon nitride (g-C3N4) based nanocomposites: Synthesis, categories, and their application in photocatalysis. *J Alloys Compd* 2020;846:156446. DOI
32. Gong Y, Li M, Wang Y. Carbon nitride in energy conversion and storage: recent advances and future prospects. *ChemSusChem* 2015;8:931-46. DOI PubMed
33. Wang X, Blechert S, Antonietti M. Polymeric graphitic carbon nitride for heterogeneous photocatalysis. *ACS Catal* 2012;2:1596-606. DOI
34. Zheng Y, Liu J, Liang J, Jaroniec M, Qiao SZ. Graphitic carbon nitride materials: controllable synthesis and applications in fuel cells and photocatalysis. *Energy Environ Sci* 2012;5:6717. DOI
35. Mo Z, Xu H, Chen Z, et al. Construction of MnO_2/Monolayer g-C_3N_4 with Mn vacancies for Z-scheme overall water splitting. *Appl Catal B-Environ* 2019;241:452-60. DOI
36. Wang Y, Xu W, Zhang Y, et al. Introducing spin polarization into atomically thin 2D carbon nitride sheets for greatly extended visible-light photocatalytic water splitting. *Nano Energy* 2021;83:105783. DOI
37. Xu Y, Fan M, Yang W, et al. Homogeneous carbon/potassium-incorporation strategy for synthesizing red polymeric carbon nitride capable of near-infrared photocatalytic H_2 production. *Adv Mater* 2021;33:e2101455. DOI PubMed
38. Yamashita H, Mori K, Kuwahara Y, et al. Single-site and nano-confined photocatalysts designed in porous materials for environmental uses and solar fuels. *Chem Soc Rev* 2018;47:8072-96. DOI PubMed
39. Chen X, Xiao S, Wang H, et al. MOFs Conferred with transient metal centers for enhanced photocatalytic activity. *Angew Chem Int Ed Engl* 2020;59:17182-6. DOI PubMed
40. Chen X, Cai Y, Liang R, et al. NH2-UiO-66(Zr) with fast electron transfer routes for breaking down nitric oxide via photocatalysis. *Appl Catal B-Environ* 2020;267:118687. DOI
41. Wen M, Li G, Liu H, Chen J, An T, Yamashita H. Metal-organic framework-based nanomaterials for adsorption and photocatalytic degradation of gaseous pollutants: recent progress and challenges. *Environ Sci : Nano* 2019;6:1006-25. DOI
42. Wen M, Mori K, Kuwahara Y, Yamashita H. Plasmonic Au@Pd nanoparticles supported on a basic metal-organic framework: synergic boosting of H_2 production from formic acid. *ACS Energy Lett* 2017;2:1-7. DOI
43. Xiao JD, Han L, Luo J, Yu SH, Jiang HL. Integration of plasmonic effects and Schottky junctions into metal-organic framework composites: steering charge flow for enhanced visible-light photocatalysis. *Angew Chem Int Ed Engl* 2018;57:1103-7. DOI PubMed
44. Dong D, Yan C, Huang J, et al. An electron-donating strategy to guide the construction of MOF photocatalysts toward co-catalyst-free highly efficient photocatalytic H_2 evolution. *J Mater Chem A* 2019;7:24180-5. DOI
45. Sun K, Liu M, Pei J, et al. Incorporating transition-metal phosphides into metal-organic frameworks for enhanced photocatalysis. *Angew Chem Int Ed Engl* 2020;59:22749-55. DOI PubMed
46. Meng X, Sheng J, Tang H, Sun X, Dong H, Zhang F. Metal-organic framework as nanoreactors to co-incorporate carbon nanodots

and CdS quantum dots into the pores for improved H2 evolution without noble-metal cocatalyst. *Appl Catal B-Environ* 2019;244:340-6. DOI

47. Lin C, Han C, Zhang H, et al. Porphyrin-based metal-organic frameworks for efficient photocatalytic H_2 production under visible-light irradiation. *Inorg Chem* 2021;60:3988-95. DOI PubMed
48. Lyle SJ, Waller PJ, Yaghi OM. Covalent organic frameworks: organic chemistry extended into two and three dimensions. *Trends Chem* 2019;1:172-84. DOI
49. Geng K, He T, Liu R, et al. Covalent organic frameworks: design, synthesis, and functions. *Chem Rev* 2020;120:8814-933. DOI PubMed
50. Segura JL, Mancheño MJ, Zamora F. Covalent organic frameworks based on Schiff-base chemistry: synthesis, properties and potential applications. *Chem Soc Rev* 2016;45:5635-71. DOI PubMed
51. Gao C, Li J, Yin S, et al. Isostructural three-dimensional covalent organic frameworks. *Angew Chem Int Ed Engl* 2019;58:9770-5. DOI PubMed
52. Jiang L, Tian Y, Sun T, et al. A Crystalline polyimide porous organic framework for selective adsorption of acetylene over ethylene. *J Am Chem Soc* 2018;140:15724-30. DOI PubMed
53. Li LH, Feng XL, Cui XH, Ma YX, Ding SY, Wang W. Salen-based covalent organic framework. *J Am Chem Soc* 2017;139:6042-5. DOI PubMed
54. Yan S, Guan X, Li H, et al. Three-dimensional Salphen-based covalent-organic frameworks as catalytic antioxidants. *J Am Chem Soc* 2019;141:2920-4. DOI PubMed
55. Lin G, Ding H, Yuan D, Wang B, Wang C. A pyrene-based, fluorescent three-dimensional covalent organic framework. *J Am Chem Soc* 2016;138:3302-5. DOI PubMed
56. Wang P, Zhou F, Zhang C, et al. Ultrathin two-dimensional covalent organic framework nanoprobe for interference-resistant two-photon fluorescence bioimaging. *Chem Sci* 2018;9:8402-8. DOI PubMed PMC
57. Das G, Biswal BP, Kandambeth S, et al. Chemical sensing in two dimensional porous covalent organic nanosheets. *Chem Sci* 2015;6:3931-9. DOI PubMed PMC
58. Ding H, Li J, Xie G, et al. An AIEgen-based 3D covalent organic framework for white light-emitting diodes. *Nat Commun* 2018;9:5234. DOI PubMed PMC
59. Bessinger D, Ascherl L, Auras F, Bein T. Spectrally switchable photodetection with near-infrared-absorbing covalent organic frameworks. *J Am Chem Soc* 2017;139:12035-42. DOI PubMed PMC
60. Wang S, Wang Q, Shao P, et al. Exfoliation of covalent organic frameworks into few-layer redox-active nanosheets as cathode materials for lithium-ion batteries. *J Am Chem Soc* 2017;139:4258-61. DOI PubMed
61. Du Y, Yang H, Whiteley JM, et al. Ionic covalent organic frameworks with spiroborate linkage. *Angew Chem Int Ed Engl* 2016;55:1737-41. DOI PubMed
62. Mulzer CR, Shen L, Bisbey RP, et al. Superior charge storage and power density of a conducting polymer-modified covalent organic framework. *ACS Cent Sci* 2016;2:667-73. DOI PubMed PMC
63. Xie J, Shevlin SA, Ruan Q, et al. Efficient visible light-driven water oxidation and proton reduction by an ordered covalent triazine-based framework. *Energy Environ Sci* 2018;11:1617-24. DOI
64. Chen R, Wang Y, Ma Y, et al. Rational design of isostructural 2D porphyrin-based covalent organic frameworks for tunable photocatalytic hydrogen evolution. *Nat Commun* 2021;12:1354. DOI PubMed PMC
65. Zhou T, Wang L, Huang X, et al. PEG-stabilized coaxial stacking of two-dimensional covalent organic frameworks for enhanced photocatalytic hydrogen evolution. *Nat Commun* 2021;12:3934. DOI PubMed PMC
66. Yang J, Acharjya A, Ye MY, et al. Protonated imine-linked covalent organic frameworks for photocatalytic hydrogen evolution. *Angew Chem Int Ed Engl* 2021;60:19797-803. DOI PubMed PMC
67. Cheng Z, Qi W, Pang CH, et al. Recent advances in transition metal nitride-based materials for photocatalytic applications. *Adv Funct Materials* 2021;31:2100553. DOI
68. Xiao J, Vequizo JJM, Hisatomi T, et al. Simultaneously tuning the defects and surface properties of Ta_3N_5 nanoparticles by Mg-Zr codoping for significantly accelerated photocatalytic H_2 evolution. *J Am Chem Soc* 2021;143:10059-64. DOI PubMed
69. Wang Z, Luo Y, Hisatomi T, et al. Sequential cocatalyst decoration on $BaTaO_2N$ towards highly-active Z-scheme water splitting. *Nat Commun* 2021;12:1005. DOI PubMed PMC
70. Wang Y, Zhao J, Chen Z, et al. Construction of Z-scheme $MoSe_2$/CdSe hollow nanostructure with enhanced full spectrum photocatalytic activity. *Appl Catal B-Environ* 2019;244:76-86. DOI
71. Zhang G, Wang X. Oxysulfide semiconductors for photocatalytic overall water splitting with visible light. *Angew Chem Int Ed Engl* 2019;58:15580-2. DOI PubMed
72. Pan R, Hu M, Liu J, et al. Two-dimensional all-in-one sulfide monolayers driving photocatalytic overall water splitting. *Nano Lett* 2021;21:6228-36. DOI PubMed
73. Chen X, Shi R, Chen Q, et al. Three-dimensional porous g-C_3N_4 for highly efficient photocatalytic overall water splitting. *Nano Energy* 2019;59:644-50. DOI
74. Lin Y, Su W, Wang X, Fu X, Wang X. LaOCl-coupled polymeric carbon nitride for overall water splitting through a one-photon excitation pathway. *Angew Chem Int Ed Engl* 2020;59:20919-23. DOI PubMed
75. Chen X, Wang J, Chai Y, Zhang Z, Zhu Y. Efficient photocatalytic overall water splitting induced by the giant internal electric field of a g-C_3N_4/rGO/PDIP Z-scheme heterojunction. *Adv Mater* 2021;33:e2007479. DOI
76. Wu C, Xue S, Qin Z, et al. Making g-C_3N_4 ultra-thin nanosheets active for photocatalytic overall water splitting. *Appl Catal B-*

Environ 2021;282:119557. DOI

77. Zhao D, Wang Y, Dong C, et al. Boron-doped nitrogen-deficient carbon nitride-based Z-scheme heterostructures for photocatalytic overall water splitting. *Nat Energy* 2021;6:388-97. DOI
78. Zhang J, Bai T, Huang H, et al. Metal-organic-framework-based photocatalysts optimized by spatially separated cocatalysts for overall water splitting. *Adv Mater* 2020;32:e2004747. DOI PubMed
79. Hu H, Wang Z, Cao L, et al. Metal-organic frameworks embedded in a liposome facilitate overall photocatalytic water splitting. *Nat Chem* 2021;13:358-66. DOI PubMed
80. Wang Y, Wu Y, Sun K, Mi Z. A quadruple-band metal-nitride nanowire artificial photosynthesis system for high efficiency photocatalytic overall solar water splitting. *Mater Horiz* 2019;6:1454-62. DOI
81. Pan Z, Zhang G, Wang X. Polymeric carbon nitride/reduced graphene oxide/Fe_2O_3: all-solid-state Z-scheme system for photocatalytic overall water splitting. *Angew Chem Int Ed Engl* 2019;58:7102-6. DOI
82. Oshima T, Nishioka S, Kikuchi Y, et al. An artificial Z-scheme constructed from dye-sensitized metal oxide nanosheets for visible light-driven overall water splitting. *J Am Chem Soc* 2020;142:8412-20. DOI PubMed
83. Zhao Y, Ding C, Zhu J, et al. A hydrogen farm strategy for scalable solar hydrogen production with particulate photocatalysts. *Angew Chem Int Ed Engl* 2020;59:9653-8. DOI PubMed
84. Takata T, Jiang J, Sakata Y, et al. Photocatalytic water splitting with a quantum efficiency of almost unity. *Nature* 2020;581:411-4. DOI PubMed
85. Zhang Z, Liu Y, Fang Y, et al. Near-infrared-plasmonic energy upconversion in a nonmetallic heterostructure for efficient H_2 evolution from ammonia borane. *Adv Sci (Weinh)* 2018;5:1800748. DOI PubMed PMC
86. Zhang MY, Li JK, Wang R, Zhao SN, Zang SQ, Mak TCW. Construction of core-shell MOF@COF hybrids with controllable morphology adjustment of COF shell as a novel platform for photocatalytic cascade reactions. *Adv Sci (Weinh)* 2021;8:e2101884. DOI PubMed PMC
87. Cao S, Chen Y, Wang H, et al. Ultrasmall CoP nanoparticles as efficient cocatalysts for photocatalytic formic acid dehydrogenation. *Joule* 2018;2:549-57. DOI
88. Zhang S, Li M, Zhao J, et al. Plasmonic AuPd-based Mott-Schottky photocatalyst for synergistically enhanced hydrogen evolution from formic acid and aldehyde. *Appl Catal B-Environ* 2019;252:24-32. DOI
89. Wang C, Sun Z, Zheng Y, Hu YH. Recent progress in visible light photocatalytic conversion of carbon dioxide. *J Mater Chem A* 2019;7:865-87. DOI
90. Hu Y. Advances in CO_2 conversion and utilization. Washington: American Chemical Society; 2010.
91. Mao J, Li K, Peng T. Recent advances in the photocatalytic CO_2 reduction over semiconductors. *Catal Sci Technol* 2013;3:2481. DOI
92. Shi R, Waterhouse GI, Zhang T. Recent progress in photocatalytic CO_2 reduction over perovskite oxides. *Sol RRL* 2017;1:1700126. DOI
93. Duan X, Xu J, Wei Z, et al. Metal-free carbon materials for CO_2 electrochemical reduction. *Adv Mater* 2017;29:1701784. DOI PubMed
94. Leitner W. The coordination chemistry of carbon dioxide and its relevance for catalysis: a critical survey. *Coord Chem Rev* 1996;153:257-84. DOI
95. Zhang L, Zhao ZJ, Gong J. Nanostructured materials for heterogeneous electrocatalytic CO_2 reduction and their related reaction mechanisms. *Angew Chem Int Ed Engl* 2017;56:11326-53. DOI PubMed
96. Shen H, Peppel T, Strunk J, Sun Z. Photocatalytic reduction of CO_2 by metal-free-based materials: recent advances and future perspective. *Sol RRL* 2020;4:1900546. DOI
97. Sun Z, Talreja N, Tao H, et al. Catalysis of carbon dioxide photoreduction on nanosheets: fundamentals and challenges. *Angew Chem Int Ed Engl* 2018;57:7610-27. DOI PubMed
98. Habisreutinger SN, Schmidt-Mende L, Stolarczyk JK. Photocatalytic reduction of CO_2 on TiO_2 and other semiconductors. *Angew Chem Int Ed Engl* 2013;52:7372-408. DOI PubMed
99. Inoue T, Fujishima A, Konishi S, Honda K. Photoelectrocatalytic reduction of carbon dioxide in aqueous suspensions of semiconductor powders. *Nature* 1979;277:637-8. DOI
100. Morris AJ, Meyer GJ, Fujita E. Molecular approaches to the photocatalytic reduction of carbon dioxide for solar fuels. *Acc Chem Res* 2009;42:1983-94. DOI PubMed
101. Angamuthu R, Byers P, Lutz M, Spek AL, Bouwman E. Electrocatalytic CO_2 conversion to oxalate by a copper complex. *Science* 2010;327:313-5. DOI PubMed
102. Li J, Shao W, Geng M, Wan S, Ou M, Chen Y. Combined Schottky junction and doping effect in $Cd_xZn_{1-x}S$@Au/$BiVO_4$ Z-Scheme photocatalyst with boosted carriers charge separation for CO_2 reduction by H_2O. *J Colloid Interface Sci* 2022;606:1469-76. DOI PubMed
103. Ou M, Tu W, Yin S, et al. Amino-assisted anchoring of $CsPbBr_3$ perovskite quantum dots on porous g-C_3N_4 for enhanced photocatalytic CO_2 reduction. *Angew Chem Int Ed Engl* 2018;57:13570-4. DOI PubMed
104. Zhang Q, Han W, Hong Y, Yu J. Photocatalytic reduction of CO_2 with H_2O on Pt-loaded TiO_2 catalyst. *Catalysis Today* 2009;148:335-40. DOI
105. Xie S, Wang Y, Zhang Q, Deng W, Wang Y. MgO- and Pt-promoted TiO_2 as an efficient photocatalyst for the preferential reduction of carbon dioxide in the presence of water. *ACS Catal* 2014;4:3644-53. DOI
106. Sorcar S, Hwang Y, Lee J, et al. CO_2, water, and sunlight to hydrocarbon fuels: a sustained sunlight to fuel (Joule-to-Joule)

photoconversion efficiency of 1%. *Energy Environ Sci* 2019;12:2685-96. DOI

107. Li N, Wang B, Si Y, et al. Toward high-value hydrocarbon generation by photocatalytic reduction of CO_2 in water vapor. *ACS Catal* 2019;9:5590-602. DOI
108. Yuan L, Hung S, Tang Z, Chen HM, Xiong Y, Xu Y. Dynamic evolution of atomically dispersed Cu species for CO_2 photoreduction to solar fuels. *ACS Catal* 2019;9:4824-33. DOI
109. Wang Q, Warnan J, Rodríguez-jiménez S, et al. Molecularly engineered photocatalyst sheet for scalable solar formate production from carbon dioxide and water. *Nat Energy* 2020;5:703-10. DOI
110. Wang C, Zhao Y, Xu H, et al. Efficient Z-scheme photocatalysts of ultrathin g-C_3N_4-wrapped Au/TiO_2-nanocrystals for enhanced visible-light-driven conversion of CO_2 with H_2O. *Appl Catal B-Environ* 2020;263:118314. DOI
111. Wang S, Teramura K, Hisatomi T, et al. Dual Ag/Co cocatalyst synergism for the highly effective photocatalytic conversion of CO_2 by H_2O over Al-$SrTiO_3$. *Chem Sci* 2021;12:4940-8. DOI PubMed PMC
112. Wang W, Deng C, Xie S, et al. Photocatalytic C-C coupling from carbon dioxide reduction on copper oxide with mixed-valence copper(I)/copper(II). *J Am Chem Soc* 2021;143:2984-93. DOI PubMed
113. Lu M, Liu J, Li Q, et al. Rational design of crystalline covalent organic frameworks for efficient CO_2 photoreduction with H_2O. *Angew Chem Int Ed Engl* 2019;58:12392-7. DOI PubMed
114. Fang ZB, Liu TT, Liu J, et al. Boosting interfacial charge-transfer kinetics for efficient overall CO_2 photoreduction via rational design of coordination spheres on metal-organic frameworks. *J Am Chem Soc* 2020;142:12515-23. DOI PubMed
115. Dong LZ, Zhang L, Liu J, et al. Stable heterometallic cluster-based organic framework catalysts for artificial photosynthesis. *Angew Chem Int Ed Engl* 2020;59:2659-63. DOI PubMed
116. Feng X, Pi Y, Song Y, et al. Metal-organic frameworks significantly enhance photocatalytic hydrogen evolution and CO_2 reduction with earth-abundant copper photosensitizers. *J Am Chem Soc* 2020;142:690-5. DOI PubMed
117. Jiang Z, Xu X, Ma Y, et al. Filling metal-organic framework mesopores with TiO_2 for CO_2 photoreduction. *Nature* 2020;586:549-54. DOI PubMed
118. Yu F, Jing X, Wang Y, Sun M, Duan C. Hierarchically porous metal-organic framework/MoS_2 interface for selective photocatalytic conversion of CO_2 with H_2O into CH_3COOH. *Angew Chem Int Ed Engl* 2021;60:24849-53. DOI
119. Wu H, Kong XY, Wen X, et al. Metal-organic framework decorated cuprous oxide nanowires for long-lived charges applied in selective photocatalytic CO_2 reduction to CH_4. *Angew Chem Int Ed Engl* 2021;60:8455-9. DOI PubMed
120. Li L, Guo H, Yao G, et al. Visible/infrared light-driven high-efficiency CO_2 conversion into ethane based on a B-Co synergistic catalyst. *J Mater Chem A* 2020;8:22327-34. DOI
121. Li R, Cheng W, Richter MH, et al. Unassisted highly selective gas-phase CO_2 reduction with a plasmonic Au/p-GaN photocatalyst using H_2O as an electron donor. *ACS Energy Lett* 2021;6:1849-56. DOI
122. Wang Y, Zhang Z, Zhang L, et al. Visible-light driven overall conversion of CO_2 and H_2O to CH_4 and O_2 on 3D-SiC@2D-MoS_2 heterostructure. *J Am Chem Soc* 2018;140:14595-8. DOI PubMed
123. Ren X, Gao M, Zhang Y, et al. Photocatalytic reduction of CO_2 on BiOX: effect of halogen element type and surface oxygen vacancy mediated mechanism. *Appl Catal B-Environ* 2020;274:119063. DOI
124. Wu CY, Lee CJ, Yu YH, et al. Efficacious CO_2 photoconversion to C_2 and C_3 hydrocarbons on upright SnS-SnS_2 heterojunction nanosheet frameworks. *ACS Appl Mater Interfaces* 2021;13:4984-92. DOI PubMed
125. Thampi KR, Kiwi J, Grätzel M. Methanation and photo-methanation of carbon dioxide at room temperature and atmospheric pressure. *Nature* 1987;327:506-8. DOI
126. Ahmed N, Shibata Y, Taniguchi T, Izumi Y. Photocatalytic conversion of carbon dioxide into methanol using zinc-copper-M(III) (M=aluminum, gallium) layered double hydroxides. *J Catal* 2011;279:123-35. DOI
127. Jelle AA, Ghuman KK, O'brien PG, et al. Highly efficient ambient temperature CO_2 photomethanation catalyzed by nanostructured RuO_2 on silicon photonic crystal support. *Adv Energy Mater* 2018;8:1702277. DOI
128. Wang L, Ghoussoub M, Wang H, et al. Photocatalytic hydrogenation of carbon dioxide with high selectivity to methanol at atmospheric pressure. *Joule* 2018;2:1369-81. DOI
129. Yan T, Wang L, Liang Y, et al. Polymorph selection towards photocatalytic gaseous CO_2 hydrogenation. *Nat Commun* 2019;10:2521. DOI PubMed PMC
130. Yan T, Li N, Wang L, et al. Bismuth atom tailoring of indium oxide surface frustrated Lewis pairs boosts heterogeneous CO_2 photocatalytic hydrogenation. *Nat Commun* 2020;11:6095. DOI PubMed PMC
131. Huang H, Mao M, Zhang Q, et al. Solar-light-driven CO_2 reduction by CH_4 on silica-cluster-modified Ni nanocrystals with a high solar-to-fuel efficiency and excellent durability. *Adv Energy Mater* 2018;8:1702472. DOI
132. Zhou L, Martirez JMP, Finzel J, et al. Light-driven methane dry reforming with single atomic site antenna-reactor plasmonic photocatalysts. *Nat Energy* 2020;5:61-70. DOI
133. Shoji S, Peng X, Yamaguchi A, et al. Photocatalytic uphill conversion of natural gas beyond the limitation of thermal reaction systems. *Nat Catal* 2020;3:148-53. DOI
134. Zhao YX, Yang B, Li HF, et al. Photoassisted selective steam and dry reforming of methane to syngas catalyzed by rhodium-vanadium bimetallic oxide cluster anions at room temperature. *Angew Chem Int Ed Engl* 2020;59:21216-23. DOI PubMed
135. Wang X, Zhao X, Zhang D, Li G, Li H. Microwave irradiation induced UIO-66-NH2 anchored on graphene with high activity for photocatalytic reduction of CO_2. *Appl Catal B-Environ* 2018;228:47-53. DOI
136. Wang Y, Wang S, Lou XWD. Dispersed nickel cobalt oxyphosphide nanoparticles confined in multichannel hollow carbon fibers for photocatalytic CO_2 reduction. *Angew Chem Int Ed Engl* 2019;58:17236-40. DOI PubMed

137. Wang G, He CT, Huang R, Mao J, Wang D, Li Y. Photoinduction of Cu single atoms decorated on UiO-66-NH_2 for enhanced photocatalytic reduction of CO_2 to Liquid fuels. *J Am Chem Soc* 2020;142:19339-45. DOI PubMed
138. Yang W, Wang HJ, Liu RR, et al. Tailoring crystal facets of metal-organic layers to enhance photocatalytic activity for CO_2 reduction. *Angew Chem Int Ed Engl* 2021;60:409-14. DOI PubMed
139. Li J, Huang H, Xue W, et al. Self-adaptive dual-metal-site pairs in metal-organic frameworks for selective CO_2 photoreduction to CH_4. *Nat Catal* 2021;4:719-29. DOI
140. Qi X, Zhong R, Chen M, et al. Single Metal-organic cage decorated with an Ir(III) complex for CO_2 photoreduction. *ACS Catal* 2021;11:7241-8. DOI
141. Liu J, Li N, Sun J, et al. Ferrocene-functionalized polyoxo-titanium cluster for CO_2 photoreduction. *ACS Catal* 2021;11:4510-9. DOI
142. Zhu S, Chen X, Li Z, et al. Cooperation between inside and outside of TiO_2: Lattice Cu^+ accelerates carrier migration to the surface of metal copper for photocatalytic CO_2 reduction. *Appl Catal B-Environ* 2020;264:118515. DOI
143. Campos-Martin JM, Blanco-Brieva G, Fierro JL. Hydrogen peroxide synthesis: an outlook beyond the anthraquinone process. *Angew Chem Int Ed Engl* 2006;45:6962-84. DOI PubMed
144. Sato K, Aoki M, Noyori R. A "Green" route to adipic acid: direct oxidation of cyclohexenes with 30 percent hydrogen peroxide. *Science* 1998;281:1646-7. DOI PubMed
145. Zhan W, Ji L, Ge Z, Wang X, Li R. A continuous-flow synthesis of primary amides from hydrolysis of nitriles using hydrogen peroxide as oxidant. *Tetrahedron* 2018;74:1527-32. DOI
146. Ksibi M. Chemical oxidation with hydrogen peroxide for domestic wastewater treatment. *Chem Eng J* 2006;119:161-5. DOI
147. Gurram RN, Al-Shannag M, Lecher NJ, Duncan SM, Singsaas EL, Alkasrawi M. Bioconversion of paper mill sludge to bioethanol in the presence of accelerants or hydrogen peroxide pretreatment. *Bioresour Technol* 2015;192:529-39. DOI PubMed
148. Yamazaki S, Siroma Z, Senoh H, Ioroi T, Fujiwara N, Yasuda K. A fuel cell with selective electrocatalysts using hydrogen peroxide as both an electron acceptor and a fuel. *J Power Sources* 2008;178:20-5. DOI
149. Chen X, Kondo Y, Kuwahara Y, Mori K, Louis C, Yamashita H. Metal-organic framework-based nanomaterials for photocatalytic hydrogen peroxide production. *Phys Chem Chem Phys* 2020;22:14404-14. DOI PubMed
150. Haider Z, Cho H, Moon G, Kim H. Minireview: Selective production of hydrogen peroxide as a clean oxidant over structurally tailored carbon nitride photocatalysts. *Catalysis Today* 2019;335:55-64. DOI
151. Su J, Vayssieres L. A place in the sun for artificial photosynthesis? *ACS Energy Lett* 2016;1:121-35. DOI
152. Lewis NS. Developing a scalable artificial photosynthesis technology through nanomaterials by design. *Nat Nanotechnol* 2016;11:1010-9. DOI PubMed
153. Faunce TA, Lubitz W, Rutherford AW, et al. Energy and environment policy case for a global project on artificial photosynthesis. *Energy Environ Sci* 2013;6:695. DOI
154. Yang Y, Zeng Z, Zeng G, et al. Ti_3C_2 Mxene/porous g-C_3N_4 interfacial Schottky junction for boosting spatial charge separation in photocatalytic H_2O_2 production. *Appl Catal B-Environ* 2019;258:117956. DOI
155. Wu S, Yu H, Chen S, Quan X. Enhanced photocatalytic H_2O_2 production over carbon nitride by doping and defect engineering. *ACS Catal* 2020;10:14380-9. DOI
156. Xie Y, Li Y, Huang Z, et al. Two types of cooperative nitrogen vacancies in polymeric carbon nitride for efficient solar-driven H_2O_2 evolution. *Appl Catal B-Environ* 2020;265:118581. DOI
157. Zhang P, Tong Y, Liu Y, et al. Heteroatom dopants promote two-electron O_2 reduction for photocatalytic production of H_2O_2 on polymeric carbon nitride. *Angew Chem Int Ed Engl* 2020;59:16209-17. DOI PubMed
158. Zhou L, Lei J, Wang F, et al. Carbon nitride nanotubes with in situ grafted hydroxyl groups for highly efficient spontaneous H_2O_2 production. *Appl Catal B-Environ* 2021;288:119993. DOI
159. Chen L, Chen C, Yang Z, Li S, Chu C, Chen B. Simultaneously tuning band structure and oxygen reduction pathway toward high-efficient photocatalytic hydrogen peroxide production using cyano-rich graphitic carbon nitride. *Adv Funct Mater* 2021;31:2105731. DOI
160. Isaka Y, Kondo Y, Kawase Y, Kuwahara Y, Mori K, Yamashita H. Photocatalytic production of hydrogen peroxide through selective two-electron reduction of dioxygen utilizing amine-functionalized MIL-125 deposited with nickel oxide nanoparticles. *Chem Commun (Camb)* 2018;54:9270-3. DOI PubMed
161. Chen X, Kuwahara Y, Mori K, Louis C, Yamashita H. Introduction of a secondary ligand into titanium-based metal-organic frameworks for visible-light-driven photocatalytic hydrogen peroxide production from dioxygen reduction. *J Mater Chem A* 2021;9:2815-21. DOI
162. Krishnaraj C, Sekhar Jena H, Bourda L, et al. Strongly Reducing (Diarylamino)benzene-based covalent organic framework for metal-free visible light photocatalytic H_2O_2 generation. *J Am Chem Soc* 2020;142:20107-16. DOI PubMed PMC
163. Mal DD, Khilari S, Pradhan D. Efficient and selective oxidation of toluene to benzaldehyde on manganese tungstate nanobars: a noble metal-free approach. *Green Chem* 2018;20:2279-89. DOI
164. Isaka Y, Kawase Y, Kuwahara Y, Mori K, Yamashita H. Two-phase system utilizing hydrophobic metal-organic frameworks (MOFs) for photocatalytic synthesis of hydrogen peroxide. *Angew Chem Int Ed Engl* 2019;58:5402-6. DOI PubMed
165. Kawase Y, Isaka Y, Kuwahara Y, Mori K, Yamashita H. Ti cluster-alkylated hydrophobic MOFs for photocatalytic production of hydrogen peroxide in two-phase systems. *Chem Commun (Camb)* 2019;55:6743-6. DOI PubMed
166. Chen X, Kuwahara Y, Mori K, Louis C, Yamashita H. A hydrophobic titanium doped zirconium-based metal organic framework for photocatalytic hydrogen peroxide production in a two-phase system. *J Mater Chem A* 2020;8:1904-10. DOI
167. Huang Y, Chong X, Liu C, Liang Y, Zhang B. Boosting hydrogen production by anodic oxidation of primary amines over a nise

nanorod electrode. *Angew Chem Int Ed Engl* 2018;57:13163-6. DOI PubMed

168. Martin A, Kalevaru VN. Heterogeneously catalyzed ammoxidation: a valuable tool for one-step synthesis of nitriles. *ChemCatChem* 2010;2:1504-22. DOI
169. Łuczak T. Electrochemical behaviour of benzylamine, 2-phenylethylamine and 4-hydroxyphenylethylamine at gold. A comparative study. *J Appl Electrochem* 2007;38:43-50. DOI
170. Fleming FF, Yao L, Ravikumar PC, Funk L, Shook BC. Nitrile-containing pharmaceuticals: efficacious roles of the nitrile pharmacophore. *J Med Chem* 2010;53:7902-17. DOI PubMed PMC
171. Wang T, Jiao N. Direct approaches to nitriles via highly efficient nitrogenation strategy through C-H or C-C bond cleavage. *Acc Chem Res* 2014;47:1137-45. DOI PubMed
172. Yan G, Zhang Y, Wang J. Recent advances in the synthesis of aryl nitrile compounds. *Adv Synth Catal* 2017;359:4068-105. DOI
173. Liu RY, Bae M, Buchwald SL. Mechanistic insight facilitates discovery of a mild and efficient copper-catalyzed dehydration of primary amides to nitriles using hydrosilanes. *J Am Chem Soc* 2018;140:1627-31. DOI PubMed PMC
174. Tian Z, Han C, Zhao Y, et al. Efficient photocatalytic hydrogen peroxide generation coupled with selective benzylamine oxidation over defective ZrS_3 nanobelts. *Nat Commun* 2021;12:2039. DOI PubMed PMC
175. Shiraishi Y, Kanazawa S, Kofuji Y, et al. Sunlight-driven hydrogen peroxide production from water and molecular oxygen by metal-free photocatalysts. *Angew Chem Int Ed Engl* 2014;53:13454-9. DOI PubMed
176. Ma R, Wang L, Wang H, et al. Solid acids accelerate the photocatalytic hydrogen peroxide synthesis over a hybrid catalyst of titania nanotube with carbon dot. *Appl Catal B-Environ* 2019;244:594-603. DOI
177. Zeng X, Liu Y, Kang Y, et al. Simultaneously tuning charge separation and oxygen reduction pathway on graphitic carbon nitride by polyethylenimine for boosted photocatalytic hydrogen peroxide production. *ACS Catal* 2020;10:3697-706. DOI
178. Zhao Y, Liu Y, Cao J, et al. Efficient production of H_2O_2 via two-channel pathway over ZIF-8/C3N4 composite photocatalyst without any sacrificial agent. *Appl Catal B-Environ* 2020;278:119289. DOI
179. Zhao Y, Liu Y, Wang Z, et al. Carbon nitride assisted 2D conductive metal-organic frameworks composite photocatalyst for efficient visible light-driven H_2O_2 production. *Appl Catal B-Environ* 2021;289:120035. DOI
180. Wu Q, Cao J, Wang X, et al. A metal-free photocatalyst for highly efficient hydrogen peroxide photoproduction in real seawater. *Nat Commun* 2021;12:483. DOI PubMed PMC
181. Teng Z, Zhang Q, Yang H, et al. Atomically dispersed antimony on carbon nitride for the artificial photosynthesis of hydrogen peroxide. *Nat Catal* 2021;4:374-84. DOI
182. Ye YX, Pan J, Xie F, et al. Highly efficient photosynthesis of hydrogen peroxide in ambient conditions. *Proc Natl Acad Sci U S A* 2021;118:e2103964118. DOI PubMed PMC